

Galaxy bispectrum, primordial non-Gaussianity and redshift space distortions

Matteo Tellarini,^a Ashley J. Ross,^{a,b} Gianmassimo Tasinato^c and David Wands^a

^aInstitute of Cosmology & Gravitation, University of Portsmouth, Dennis Sciana Building, Portsmouth, PO1 3FX, United Kingdom

^bCenter for Cosmology & AstroParticle Physics, The Ohio State University, Columbus, OH 43210, USA

^cDepartment of Physics, Swansea University, Swansea, SA2 8PP, UK

E-mail: matteo.tellarini@port.ac.uk, ross.1333@osu.edu, g.tasinato@swansea.ac.uk, david.wands@port.ac.uk

Abstract. Measurements of the non-Gaussianity of the primordial density field have the power to considerably improve our understanding of the physics of inflation. Indeed, if we can increase the precision of current measurements by an order of magnitude, a null-detection would rule out many classes of scenarios for generating primordial fluctuations. Large-scale galaxy redshift surveys represent experiments that hold the promise to realise this goal. Thus, we model the galaxy bispectrum and forecast the accuracy with which it will probe the parameter f_{NL} , which represents the degree of primordial local-type non Gaussianity. Specifically, we address the problem of modelling redshift space distortions (RSD) in the tree-level galaxy bispectrum including f_{NL} . We find novel contributions associated with RSD, with the characteristic large scale amplification induced by local-type non-Gaussianity. These RSD effects must be properly accounted for in order to obtain un-biased measurements of f_{NL} from the galaxy bispectrum. We propose an analytic template for the monopole which can be used to fit against data on large scales, extending models used in the recent measurements. Finally, we perform idealised forecasts on $\sigma_{f_{\text{NL}}}$ – the accuracy of the determination of local non-linear parameter f_{NL} – from measurements of the galaxy bispectrum. Our findings suggest that current surveys can in principle provide f_{NL} constraints competitive with *Planck*, and future surveys could improve them further.

Keywords: Primordial non-Gaussianity, Large-Scale Structure

ArXiv ePrint: [1603.06814](https://arxiv.org/abs/1603.06814)

Contents

1	Introduction	1
2	Basics	3
2.1	Perturbation theory	3
2.2	Press-Schechter approach	4
2.3	The bivariate model	5
2.4	Galaxy overdensity in the Eulerian frame	5
3	Redshift space distortions	7
3.1	Galaxy overdensity in redshift space	8
3.2	Galaxy bispectrum monopole	9
4	Fisher Analysis	12
4.1	Methodology	12
4.2	Results	14
5	Conclusions	15
A	Halo mass function and Lagrangian bias	21
B	Position-dependent power spectrum	22
C	\mathcal{D} factors	24
D	Basic numbers for BOSS, eBOSS, DESI, Euclid	26

1 Introduction

Inflation in the very early universe is a simple mechanism for generating primordial density fluctuations from vacuum fluctuations. This gives rise to anisotropies in the cosmic microwave background (CMB) and the large-scale structures that we observe in the Universe today [1]. Different realizations of inflation lead to distinctive observational consequences, which can be studied through the predicted statistics for the primordial fluctuations. An important example is the non-Gaussian features associated with the non-vanishing n -point correlations functions $\langle \Phi_{\text{in}}(\mathbf{k}_1) \dots \Phi_{\text{in}}(\mathbf{k}_n) \rangle$ of the primordial gravitational potential $\Phi_{\text{in}}(\mathbf{x})$. Reconstructing the initial non-Gaussian pattern of primordial fluctuations from inflation out of late-time observations is a major focus of current cosmology research.

Inflationary mechanisms can lead to primordial non-Gaussian features in different ways [2]: the most studied example is *local* non-Gaussianity, in which fluctuations of the primordial potential $\Phi_{\text{in}}(\mathbf{x})$ can be expressed as a power series of a single, Gaussian field $\varphi_G(\mathbf{x})$ so that [3–5]

$$\Phi_{\text{in}}(\mathbf{x}) = \varphi_G(\mathbf{x}) + f_{\text{NL}} (\varphi_G^2(\mathbf{x}) - \langle \varphi_G^2 \rangle) + \dots, \quad (1.1)$$

with a constant non-linearity parameter f_{NL} controlling the deviations from purely Gaussian statistics. In this work, we will focus our attention on local non-Gaussianity.

Local non-Gaussianity in real space leads to a primordial bispectrum for Φ_{in} (the Fourier transform of the 3-point function) which peaks in the squeezed configuration ($k_1 \simeq k_2 \gg k_3$) in Fourier space. Scenarios leading to local non-Gaussianity – and f_{NL} greater than or of order one – include multiple field inflationary models, or set-ups involving conversion mechanisms as curvaton or modulated reheating (see e.g. [6] for a review). Single field, slow-roll inflation instead predicts an extremely small non-Gaussian signal in the squeezed configuration of the bispectrum, whose size is of the order of the tilt of the power spectrum [7].

The state-of-the-art for measurements of f_{NL} is given by *Planck* satellite measurements of the CMB bispectrum [8] which gives $-9.2 < f_{\text{NL}} < 10.8$ at 95% CL. Distinguishing $|f_{\text{NL}}| \ll 1$ from $|f_{\text{NL}}| \sim 1$ is a key target to observationally distinguish single-field, slow-roll inflation from other scenarios [9]. However, CMB data alone may not be able to reach this goal, limited on large-scales by cosmic variance and on small scales by Silk damping.

A promising possibility comes from the statistics of large-scale structure (LSS), and was first pointed out in the pioneering paper by Dalal *et al* [10]. The coupling between the long and short modes present in local-type non-Gaussianity introduces a scale-dependent relation between dark matter halos and the underlying matter distribution, which scales as f_{NL}/k^2 and therefore affects the LSS power spectrum [10–13]. This contribution, induced by primordial non-Gaussianity (PNG), is amplified at large scales; the clustering of LSS objects thus offers a way to measure the non-linear parameter f_{NL} which is complementary to the CMB. By analyzing the galaxy power spectrum, constraints have already been set [12, 14–21] which are competitive with *WMAP* [22], while future redshift surveys are expected to give results more stringent than *Planck* [23–26]. Moreover, the use of multi-tracer techniques is expected to allow constraints better than the naive cosmic variance limit [27, 28]. Such techniques are promising for further improving the bounds on f_{NL} [29–32].

Studies of the galaxy bispectrum indicate that an accuracy in determining local f_{NL} of order $\sigma_{f_{\text{NL}}} \sim \text{few}$ is achievable [33–35]. The accuracy achievable could even be less than one if the survey is optimised for detecting PNG [36]. Considering such higher-order statistics gives access to the full shape information of the non-Gaussian signal, with the primordial one having a scale dependence even stronger than k^{-2} [35, 37, 38]. Additionally, information contained in the bispectrum potentially allows us to break the degeneracy in the power spectrum between f_{NL} and the next-order non-Gaussian parameter g_{NL} [39], as discussed in [37, 38].

On the other hand, there are significant challenges in measuring f_{NL} with LSS that are both theoretical and observational. At the theoretical level, as the Universe evolves density perturbations undergo non-linear evolution through gravitational collapse, and therefore we require an accurate modelling of the density evolution, capable of separating the primordial non-Gaussian signal from the one generated by clustering. Moreover, a precise description of how dark matter halos form starting from the primordial density field is necessary. Further, the high accuracy required for measuring a signal of $f_{\text{NL}} \sim 1$ implies that General Relativity (GR) effects cannot be neglected. Although in the simplest halo models they do not give rise to a scale-dependent bias [40–42], GR effects do source contributions to the squeezed limit of the matter bispectrum [43, 44] and generate secondary non-Gaussianities along the path of the photons from the emitting galaxy and the observer, in analogy with the CMB (see for instance [26, 45] and references therein).

At the observational level, several issues should be taken into account, such as mask geometry and systematic effects, which can mimic the scale dependence of PNG [46–48]. Moreover, redshift space distortions (RSD) are an additional source of complexity [49]: since the redshift measurements used to infer the distances of galaxies are contaminated by peculiar velocities, distortions appear along the line of sight. They can either be due to the in-fall of galaxies into clusters or due to the velocity dispersion inside a cluster, when its non-linear structure is resolved. The former leads to an apparent squashing of the clustering along the line of sight on large scales (say $k \lesssim 0.1 h/\text{Mpc}$), modelled at linear level through the *Kaiser factor* [50], while the latter is responsible for elongation on small scales (say $k \gtrsim 0.1 h/\text{Mpc}$), usually referred to as *Fingers of God* (FoG)¹.

In this work we address the problem of computing the galaxy bispectrum in redshift space with PNG of local type. For the purpose of obtaining an analytic result, we focus mainly on large-scale regimes. We point out new potentially significant effects, induced by primordial non-Gaussianity, associated with large-scale amplifications of RSD. By decomposing the line of sight dependence of the bispectrum into spherical harmonics, we also make a prediction for the galaxy monopole, motivated by the recent measurement of [52].

We also use a Fisher matrix analysis to estimate $\sigma_{f_{\text{NL}}}$ expected from the bispectrum of BOSS [53], eBOSS [54], DESI [55], Euclid [56]. These results are approximate, but can be compared to forecast constraint from the power spectrum [24, 57] in order to estimate the potential power of bispectrum

¹Historically, the presence of FoG was recognised for the first time in [51].

measurements in future. A comparison suggests that the bispectrum may improve the measurement of f_{NL} by about an order of magnitude respect to the power spectrum of a single tracer.

2 Basics

In this section we briefly discuss how the local non-linear parameter f_{NL} affects the evolution of the density field and the formation of structures. We review our findings of [58] and we define our notation. See also [59] for a detailed review on these topics.

We concentrate on local type non-Gaussianity of the form given in eq. (1.1). Local non-gaussianity induces correlations among fluctuations of different wave numbers, in particular between long and short modes. This becomes apparent when taking the Fourier transform of eq. (1.1): the second term proportional to f_{NL} becomes a convolution, which couples different wavenumbers of the Gaussian mode φ_{G} . This fact is important for our discussion.

2.1 Perturbation theory

The evolution equations for perturbations of a cosmic fluid in an expanding Friedman-Robertson-Walker universe can be formulated in terms of the matter overdensity $\delta(\mathbf{x})$ and the corresponding velocity divergence $\theta(x) = \nabla \cdot \mathbf{v}(\mathbf{x})$, and then solved in perturbation theory by [59]

$$\delta(\mathbf{k}, z) = \sum_{n=1}^{\infty} \int \frac{d\mathbf{k}_1}{(2\pi)^3} \cdots \int \frac{d\mathbf{k}_{n-1}}{(2\pi)^3} \int d\mathbf{k}_n \delta^D(\mathbf{k} - \cdots - \mathbf{k}_n) \mathcal{F}_n(\mathbf{k}_1, \dots, \mathbf{k}_n, z) \delta_{\text{lin}}(\mathbf{k}_1, z) \cdots \delta_{\text{lin}}(\mathbf{k}_n, z) \quad (2.1)$$

$$\begin{aligned} \theta(\mathbf{k}, z) = & -f\mathcal{H} \sum_{n=1}^{\infty} \int \frac{d\mathbf{k}_1}{(2\pi)^3} \cdots \int \frac{d\mathbf{k}_{n-1}}{(2\pi)^3} \int d\mathbf{k}_n \delta^D(\mathbf{k} - \cdots - \mathbf{k}_n) \mathcal{G}_n(\mathbf{k}_1, \dots, \mathbf{k}_n, z) \times \\ & \times \delta_{\text{lin}}(\mathbf{k}_1, z) \cdots \delta_{\text{lin}}(\mathbf{k}_n, z), \end{aligned} \quad (2.2)$$

where \mathcal{H} is the conformal Hubble parameter at redshift z , related to the Hubble parameter H by $\mathcal{H}(z) = aH$, and f is the logarithmic derivative of the linear growth factor $D(z)$, $f = d \ln D / d \ln a \approx \Omega_m^{4/7}(z)$ in Λ CDM [60]. In the matter-era $D(z) \propto (1+z)^{-1}$ and we use the normalization $D(0) = 1$. The linearly evolving density field δ_{lin} is related to the primordial gravitational potential through

$$\delta_{\text{lin}}(\mathbf{k}, z) = \alpha(k, z) \Phi_{\text{in}}(\mathbf{k}), \quad (2.3)$$

where the function $\alpha(k, z)$ is defined as

$$\alpha(k, z) \equiv \frac{2k^2 c^2 T(k) D(z)}{3\Omega_m H_0^2}. \quad (2.4)$$

$T(k)$ is the transfer function, which goes to one as $k \rightarrow 0$. Note that the linearly evolving density (eq. (2.3)) includes non-Gaussian terms in the presence of PNG. Thus it is useful to define the Gaussian part of the linearly evolving density field as

$$\delta_{\text{G}}(\mathbf{k}, z) = \alpha(k, z) \varphi_{\text{G}}(\mathbf{k}). \quad (2.5)$$

In general, the kernels \mathcal{F}_n and \mathcal{G}_n are time dependent. However, since they are weakly sensitive to the underlying cosmology, we can compute them for an Einstein-De Sitter universe, where they are constant in time. At linear order they read $\mathcal{F}_1(\mathbf{k}) = \mathcal{G}_1(\mathbf{k}) = 1$, so that $\delta^{(1)} = \delta_{\text{G}}$ and $\theta^{(1)} = -f\mathcal{H} \delta_{\text{G}}$. The second-order solutions are [59]

$$\delta^{(2)}(\mathbf{k}, z) = \int \frac{d\mathbf{k}_1}{(2\pi)^3} \int \frac{d\mathbf{k}_2}{(2\pi)^3} \delta^D(\mathbf{k} - \mathbf{k}_1 - \mathbf{k}_2) \left[\mathcal{F}_2(\mathbf{k}_1, \mathbf{k}_2) + f_{\text{NL}} \frac{\alpha(k)}{\alpha(k_1)\alpha(k_2)} \right] \delta_{\text{G}}(\mathbf{k}_1, z) \delta_{\text{G}}(\mathbf{k}_2, z) \quad (2.6)$$

$$\theta^{(2)}(\mathbf{k}, z) = -f\mathcal{H} \int \frac{d\mathbf{k}_1}{(2\pi)^3} \int \frac{d\mathbf{k}_2}{(2\pi)^3} \delta^D(\mathbf{k} - \mathbf{k}_1 - \mathbf{k}_2) \times$$

$$\times \left[\mathcal{G}_2(\mathbf{k}_1, \mathbf{k}_2) + f_{\text{NL}} \frac{\alpha(k)}{\alpha(k_1)\alpha(k_2)} \right] \delta_{\text{G}}(\mathbf{k}_1, z) \delta_{\text{G}}(\mathbf{k}_2, z) \quad (2.7)$$

with the kernels defined as

$$\mathcal{F}_2(\mathbf{k}_1, \mathbf{k}_2) = \frac{5}{7} + \frac{1}{2} \frac{\mathbf{k}_1 \cdot \mathbf{k}_2}{k_1 k_2} \left(\frac{k_1}{k_2} + \frac{k_2}{k_1} \right) + \frac{2}{7} \frac{(\mathbf{k}_1 \cdot \mathbf{k}_2)^2}{k_1^2 k_2^2}, \quad (2.8)$$

$$\mathcal{G}_2(\mathbf{k}_1, \mathbf{k}_2) = \frac{3}{7} + \frac{1}{2} \frac{\mathbf{k}_1 \cdot \mathbf{k}_2}{k_1 k_2} \left(\frac{k_1}{k_2} + \frac{k_2}{k_1} \right) + \frac{4}{7} \frac{(\mathbf{k}_1 \cdot \mathbf{k}_2)^2}{k_1^2 k_2^2}. \quad (2.9)$$

Notice that the couplings between modes of different wavelengths introduce a dependence on f_{NL} in the second order solutions (eqs. (2.6) and (2.7)).

The quantities $\delta(\mathbf{x})$ and $\theta(\mathbf{x})$ are expressed in Eulerian frame, with the initial spatial coordinate \mathbf{q} in the Lagrangian frame being related to the evolved Eulerian coordinate \mathbf{x} through the formula

$$\mathbf{x}(\mathbf{q}, \tau) = \mathbf{q} + \mathbf{\Psi}(\mathbf{q}, \tau), \quad (2.10)$$

where $\mathbf{\Psi}$ is the displacement field. Such relation is useful for obtaining an alternative way to write the second-order solution of eq. (2.6), which will be needed in section 2.4. It is given by [61, 62]:

$$\delta^{(2)}(\mathbf{x}, \tau) = \frac{17}{21} (\delta_{\text{lin}}(\mathbf{x}, z))^2 + \frac{2}{7} s^2(\mathbf{x}, z) - \mathbf{\Psi}(\mathbf{x}, z) \cdot \nabla \delta(\mathbf{x}, z), \quad (2.11)$$

where $s^2 = s_{ij} s^{ij}$ and s_{ij} is the trace-free *tidal tensor*, defined as

$$s_{ij} \equiv \left(\nabla_i \nabla_j - \frac{1}{3} \delta_{ij}^K \nabla^2 \right) \nabla^{-2} \delta, \quad (2.12)$$

and δ_{ij}^K is the Kronecker delta. From now on, in order to simplify our expressions, we will not explicitly write the redshift dependence in the density and velocity fields.

2.2 Press-Schechter approach

The Press-Schechter approach [63] and its extensions [64, 65] provide a consistent framework for describing the full non-linearly evolved density field, and in particular the number of gravitationally collapsed dark matter halos, in terms of the initial, linearly growing density field (see [66] for a pedagogical review). Dark matter halos are identified as peaks in the linearly growing density field of eq. (2.3), exceeding a suitable threshold value: this is usually assumed to be the linearly growing density amplitude for a spherically collapsed object, $\delta_c \simeq 1.686$ [1].

The number density of objects with mass M at redshift z is called the *mass function*. Defining $\nu \equiv \delta_c / \sigma$, the Press-Schechter approach predicts the mass function to have the form

$$n_g(M, z) = f(\nu) \frac{\rho_m}{M} \left| \frac{d \ln \sigma}{dM} \right|, \quad (2.13)$$

where the variance of the smoothed linearly-evolved density field is

$$\sigma^2 = \langle \delta_{\text{lin}}^2 \rangle = \int \frac{d^3 p}{(2\pi)^3} \int \frac{d^3 p'}{(2\pi)^3} W_M(p) \alpha(p, z) W_M(p') \alpha(p', z) \langle \Phi_{\text{in}}(\mathbf{p}) \Phi_{\text{in}}(\mathbf{p}') \rangle. \quad (2.14)$$

We choose the window function $W_M(k, R)$ to be the real-space top-hat filter of length scale $R(M) = (3M/4\pi\rho_m)^{1/3}$, with Fourier transform

$$W_M(k, R) = \frac{3}{(kR)^3} [\sin(kR) - kR \cos(kR)]. \quad (2.15)$$

In this work we follow [35] and assume the mass function to be a combination of the Press-Schechter f_{PS} [63], Sheth-Tormen f_{ST} [67–69] and Lo Verde f_{LV} [70] mass functions:

$$f(\nu) = f_{\text{ST}} \frac{f_{\text{LV}}}{f_{\text{PS}}} = f_{\text{ST}}(\nu) \left[1 + \frac{1}{6} \left(\kappa_3(M) H_3(\nu) - \frac{d\kappa_3(M)/dM}{d \ln \sigma^{-1}/dM} \frac{H_2(\nu)}{\nu} \right) \right], \quad (2.16)$$

where H_n is the n -th Hermite polynomial and the 3rd cumulant $\kappa_3(M)$ is approximately [71]

$$\kappa_3(M) \approx f_{\text{NL}} (6.6 \times 10^{-4}) \left[1 - 0.016 \ln \left(\frac{M}{h^{-1} M_\odot} \right) \right]. \quad (2.17)$$

Equation (2.16) is assumed to be a reasonable description of objects formed from ellipsoidal collapse with non-Gaussian (nG) initial conditions. Further details on the mass function can be found in appendix A.

2.3 The bivariate model

The fact that primordial non-Gaussianity couples modes of different wavenumber has important consequences for the Press-Schechter theory of structure formation. Since dark matter halos are associated with peaks of the matter density contrast, we can expect that the distribution of halo overdensity depends not only on the local value of the matter density contrast, but also on how it is distributed around a given position. This information is encoded in the correlation functions of the matter density contrast, that in turn are affected by PNG. A convenient way for describing this fact introduces the concept of peak-background split (PBS), and leads to important consequences when studying the overdensity of halos with PNG of local-type [10, 12, 35, 38, 58, 72, 73]. The PBS approach identifies the primordial Gaussian field φ_G as a superposition of statistically independent long and short modes

$$\varphi_G(\mathbf{q}) = \varphi_{G,l}(\mathbf{q}) + \varphi_{G,s}(\mathbf{q}), \quad (2.18)$$

where the use of \mathbf{q} indicates that we work with the initial (or linearly evolved) quantities, therefore in the Lagrangian frame.

The (arbitrary) length scale l is chosen such that the short modes are responsible for the collapse of matter into objects on a scale $R \ll l$, while the long modes only perturb the approximately homogeneous background cosmology. This in turn requires the variable ν in the mass function to be replaced with a *local* value

$$\nu = \frac{\delta_c}{\sigma} \longrightarrow \nu(\mathbf{q}) = \frac{\delta_c - \delta_{\text{lin},l}(\mathbf{q})}{\sigma_l(\mathbf{q})}, \quad (2.19)$$

where the long density modes are defined as

$$\delta_{\text{lin},l}(\mathbf{k}) = \delta_{G,l} + f_{\text{NL}} \alpha (\varphi_{G,l}^2 - \langle \varphi_{G,l}^2 \rangle) \quad (2.20)$$

and the effective variance of the short modes is now modulated, through PNG, by $\varphi_{G,l}$,

$$\sigma_l = (1 + 2f_{\text{NL}} \varphi_{G,l}) \sigma. \quad (2.21)$$

By treating $\delta_{\text{lin},l}$ and σ_l as independent perturbations controlling the halo overdensity in Lagrangian space, $\delta_g^L(\mathbf{q})$, this quantity can be then conveniently expressed as a double Taylor expansion,

$$\delta_g^L(\mathbf{q}) = \frac{n_g(\mathbf{q}) - \langle n_g \rangle}{\langle n_h \rangle} = b_{10}^L \delta_{\text{lin}} + b_{01}^L \varphi_G + b_{20}^L (\delta_{\text{lin}})^2 + b_{11}^L \delta_{\text{lin}} \varphi_G + b_{02}^L \varphi_G^2 + \dots, \quad (2.22)$$

where we dropped the subscript l in the right hand side to simplify the notation; the Lagrangian bias coefficients b_{ij}^L derived from the mass function of eq. (2.16) are quoted in appendix A. Equation (2.22) is known as the *bivariate model* for the halo/galaxy overdensity [72] (see also [74] for a recent application of a bivariate model for an effective field theory approach to galaxy biasing).

2.4 Galaxy overdensity in the Eulerian frame

The bivariate model describes the statistics of the objects in the Lagrangian frame, while their dynamics are obtained by the transformation to Eulerian coordinates. As we explained, the two frames are linked by $\mathbf{x}(\mathbf{q}, \tau) = \mathbf{q} + \Psi(\mathbf{q}, \tau)$, where the displacement field Ψ is the dynamical quantity in the Lagrangian picture. The transformation can be performed under the conservation of the number density of objects in a given volume; if there is no velocity bias between objects and matter, then [75]

$$1 + \delta_g^E(\mathbf{x}, z) = [1 + \delta(\mathbf{x}, z)] [1 + \delta_g^L(\mathbf{q}, z)]. \quad (2.23)$$

In [35, 72], the halo/galaxy overdensity in the Eulerian frame is obtained by assuming spherical collapse. By dropping this assumption, we get a more general (non-local) result [58]:

$$\delta_g^E(\mathbf{k}) = b_{10}^E \delta + b_{01}^E \varphi_G + b_{20}^E \delta * \delta + b_{11}^E \delta * \varphi_G + b_{02}^E \varphi_G * \varphi_G - \frac{2}{7} b_{10}^L s^2 - b_{01} n^2, \quad (2.24)$$

where $*$ stands for a convolution and the Eulerian bias coefficients are related to Lagrangian ones through

$$\begin{aligned} b_{10}^E &= 1 + b_{10}^L, \\ b_{01}^E &= b_{01}^L, \\ b_{20}^E &= \frac{8}{21} b_{10}^L + b_{20}^L, \\ b_{11}^E &= b_{01}^L + b_{11}^L, \\ b_{02}^E &= b_{02}^L. \end{aligned} \quad (2.25)$$

From now on, we drop the superscript E to indicate the Eulerian bias coefficients, in order to simplify the notation. However, we continue to write the superscript L where needed for avoiding confusion. As discussed in section 2.1, the Fourier transform of the density field in Eulerian coordinates is

$$\delta(\mathbf{k}) = \delta_G(\mathbf{k}) + \int \frac{d\mathbf{q}}{(2\pi)^3} \left[\mathcal{F}_2(\mathbf{q}, \mathbf{k} - \mathbf{q}) + f_{\text{NL}} \frac{\alpha(k)}{\alpha(q)\alpha(|\mathbf{k} - \mathbf{q}|)} \right] \delta_G(\mathbf{q}) \delta_G(\mathbf{k} - \mathbf{q}), \quad (2.26)$$

while the tidal term s^2 reads [76, 77]

$$s^2(\mathbf{k}) = \int \frac{d\mathbf{q}}{(2\pi)^3} \mathcal{S}_2(\mathbf{q}, \mathbf{k} - \mathbf{q}) \delta_G(\mathbf{q}) \delta_G(\mathbf{k} - \mathbf{q}), \quad (2.27)$$

with the kernel defined as follows

$$\mathcal{S}_2(\mathbf{k}_1, \mathbf{k}_2) = \frac{(\mathbf{k}_1 \cdot \mathbf{k}_2)^2}{k_1^2 k_2^2} - \frac{1}{3}. \quad (2.28)$$

The non-Gaussian shift term n^2 is a consequence of the displacement of halos/galaxies respect to their initial positions \mathbf{q} in the Lagrangian frame, which affects the field $\varphi_G(\mathbf{x})$:

$$n^2(\mathbf{k}) = 2 \int \frac{d\mathbf{q}}{(2\pi)^3} \mathcal{N}_2(\mathbf{q}, \mathbf{k} - \mathbf{q}) \frac{\delta_G(\mathbf{q}) \delta_G(\mathbf{k} - \mathbf{q})}{\alpha(|\mathbf{k} - \mathbf{q}|)}, \quad (2.29)$$

where the kernel is

$$\mathcal{N}_2(\mathbf{k}_1, \mathbf{k}_2) = \frac{\mathbf{k}_1 \cdot \mathbf{k}_2}{2k_1^2}. \quad (2.30)$$

We use the following standard definitions for the galaxy power spectrum P_{gg} and bispectrum B_{ggg} :

$$\begin{aligned} \langle \delta_g^E(\mathbf{k}_1) \delta_g^E(\mathbf{k}_2) \rangle &= (2\pi)^3 \delta^D(\mathbf{k}_1 + \mathbf{k}_2) P_{gg}(\mathbf{k}_1), \\ \langle \delta_g^E(\mathbf{k}_1) \delta_g^E(\mathbf{k}_2) \delta_g^E(\mathbf{k}_3) \rangle &= (2\pi)^3 \delta^D(\mathbf{k}_1 + \mathbf{k}_2 + \mathbf{k}_3) B_{ggg}(\mathbf{k}_1, \mathbf{k}_2, \mathbf{k}_3). \end{aligned}$$

At tree-level, they can be conveniently written as

$$P_{gg}(\mathbf{k}_1) = E_1^2(\mathbf{k}_1) P(k_1), \quad (2.31)$$

$$B_{ggg}(\mathbf{k}_1, \mathbf{k}_2, \mathbf{k}_3) = 2E_1(\mathbf{k}_1) E_1(\mathbf{k}_2) E_2(\mathbf{k}_1, \mathbf{k}_2) P(k_1) P(k_2) + 2 \text{ cyc.}, \quad (2.32)$$

where $P(k)$ is the matter power spectrum for the Gaussian source field φ_G , while the kernels E_i are defined as

$$E_1(\mathbf{k}_1) = b_{10} + \frac{b_{01}}{\alpha(k_1)} \quad (2.33)$$

$$\begin{aligned}
E_2(\mathbf{k}_1, \mathbf{k}_2) = & b_{10} \left[F_2(\mathbf{k}_1, \mathbf{k}_2) + f_{\text{NL}} \frac{\alpha(|\mathbf{k}_1 + \mathbf{k}_2|)}{\alpha(k_1)\alpha(k_2)} \right] + \left[b_{20} - \frac{2}{7} b_{10}^{\text{L}} S_2(\mathbf{k}_1, \mathbf{k}_2) \right] \\
& + \frac{b_{11}}{2} \left[\frac{1}{\alpha(k_1)} + \frac{1}{\alpha(k_2)} \right] + \frac{b_{02}}{\alpha(k_1)\alpha(k_2)} - b_{01} \left[\frac{N_2(\mathbf{k}_1, \mathbf{k}_2)}{\alpha(k_2)} + \frac{N_2(\mathbf{k}_2, \mathbf{k}_1)}{\alpha(k_1)} \right].
\end{aligned} \tag{2.34}$$

The term $b_{01}/\alpha(k_1) \propto f_{\text{NL}}/k_1^2$ in E_1 is the so-called scale-dependent bias: it is responsible for deviations on the large-scale clustering, with respect to the scale-independent bias b_{10} . The first and second term that appears in E_2 account for non-linear clustering and non-linear biasing respectively, while the terms in the bottom line describe the non-linear effects due to PNG. A detailed analysis of the results for the bispectrum is presented in [58].

To conclude this section, let us point out that for avoiding the complexities of a full bispectrum measurement, a new observable is proposed in [78] in terms of position dependent power spectrum. We explore this possibility in appendix B, in light of the result of eq. (2.32).

3 Redshift space distortions

The peculiar velocities of galaxies contaminate the redshift measurements of surveys, resulting in distortions along the line of sight. The in-fall of galaxies into clusters is responsible for large-scale distortions, while the velocity dispersion inside a cluster leads to the Fingers of God (FoG), usually a small-scale effect. In this paper, for the first time, we study how PNG affects the bivariate halo distribution when formulated in redshift space, finding new and potentially sizeable large scale effects. We model RSD within a perturbative approach and focus mainly on the large scale effects, for the purpose of obtaining analytic results.

An object at some position \mathbf{x} and redshift z appears in redshift space at position [79]:

$$\begin{aligned}
\mathbf{x}_s(z) = & \mathbf{x} + (1+z) \frac{\mathbf{v}(\mathbf{x}) \cdot \hat{x}}{H(z)} \hat{x} = \mathbf{x} + \frac{v_x(\mathbf{x})}{\mathcal{H}(z)} \hat{x} \\
\approx & \mathbf{x} + f u_z(\mathbf{x}) \hat{z}.
\end{aligned} \tag{3.1}$$

In the second line we use $f \equiv d \ln D / d \ln a$, and we introduce the reduced component along the line of sight, u_z , given by

$$u_z(\mathbf{k}) = \mathbf{u}(\mathbf{k}) \cdot \hat{z} = -\frac{i\mu}{k} \frac{\theta(\mathbf{k})}{f\mathcal{H}} = \frac{i\mu}{k} \eta(\mathbf{k}), \tag{3.2}$$

where $\mu \equiv \hat{k} \cdot \hat{z} = \mathbf{k} \cdot \hat{z} / k$. The second line of eq. (3.1) holds under the *plane parallel* (or *distant observer*, or *flat sky*) approximation. If the distances between galaxies are much smaller than the distance between the observer and the galaxies (resulting therefore in a small transverse component with respect to the radial direction) the line of sight \hat{x} can be assumed to be fixed along \hat{z} , pointing towards the centre of the galaxies of interest. When used to compute the galaxy power spectrum, this approximation has been shown to be valid for pairs separated by an angle less than 10° [80]. If one has to use the full data from surveys such as BOSS and Euclid, where distances between galaxies can be comparable with the observer distance, then wide angle effects must be considered as well. This problem has been addressed in several works with various approaches (see for instance [80–88]), investigated in numerical simulations (for example in [89]) and the impact on measurements considered [90, 91]. However, in this first work about the effect of PNG on the bispectrum in redshift space, as predicted by the bivariate model, we will neglect for simplicity wide angle effects. Since we will show that PNG could be enhanced by RSD on large scales, in regimes where wide angle effects may not be negligible, the results of section 3 should be considered as a zero order approximation of a more general framework which combines PNG, RSD and wide angle effects. The development of this framework is left for future work.

Equation (3.2) approximates the redshift space mapping of eq. (3.1) as a power series. By comparing eq. (3.2) with eq. (2.2), it follows that

$$\eta(\mathbf{k}) = \sum_{n=1}^{\infty} \int \frac{d\mathbf{k}_1}{(2\pi)^3} \cdots \int \frac{d\mathbf{k}_{n-1}}{(2\pi)^3} \int d\mathbf{k}_n \delta^D(\mathbf{k} - \mathbf{k}_1 - \dots - \mathbf{k}_n) \mathcal{G}_n(\mathbf{k}_1, \dots, \mathbf{k}_n) \delta_{\text{lin}}(\mathbf{k}_1) \cdots \delta_{\text{lin}}(\mathbf{k}_n). \tag{3.3}$$

3.1 Galaxy overdensity in redshift space

The transformation from real to redshift space is obtained by requiring the conservation of the number density of objects,

$$[1 + \delta_g^s(\mathbf{x}_s)]d\mathbf{x}_s = [1 + \delta_g^E(\mathbf{x})]d\mathbf{x}, \quad (3.4)$$

so that in Fourier space we have [92]

$$\delta_g^s(\mathbf{k}) = \int d\mathbf{x}_s \delta_g^s(\mathbf{x}_s) e^{-i\mathbf{k}\cdot\mathbf{x}_s} \quad (3.5)$$

$$= \int d\mathbf{x} [\delta_g^E(\mathbf{x}) + 1] e^{-i\mathbf{k}\cdot(\mathbf{x} + f u_z(\mathbf{x})\hat{z})} - \int d\mathbf{x} e^{-i\mathbf{k}\cdot\mathbf{x}} \quad (3.6)$$

$$= \delta_g^E(\mathbf{k}) + \int d\mathbf{x} e^{-i\mathbf{k}\cdot\mathbf{x}} \left(e^{-ifk_z u_z(\mathbf{x})} - 1 \right) [\delta_g^E(\mathbf{x}) + 1] \quad (3.7)$$

$$= \delta_g^E(\mathbf{k}) - \int d\mathbf{x} e^{-i\mathbf{k}\cdot\mathbf{x}} \left(ifk_z u_z(\mathbf{x}) + \frac{1}{2} f^2 k_z^2 u_z^2(\mathbf{x}) + \dots \right) [\delta_g^E(\mathbf{x}) + 1] \quad (3.8)$$

$$= \delta_g^E(\mathbf{k}) + f\mu^2 \eta(\mathbf{k}) - \int d\mathbf{x} e^{-i\mathbf{k}\cdot\mathbf{x}} \left(ifk_z u_z(\mathbf{x}) \delta_g(\mathbf{x}) + \frac{1}{2} f^2 k_z^2 u_z^2(\mathbf{x}) + \dots \right), \quad (3.9)$$

where eq. (3.8) holds under the assumption of a small velocity component along the line of sight, $|u_z| \ll 1$.

In general, the redshift-space galaxy overdensity can be written as

$$\delta_g^s(\mathbf{k}) = \sum_{n=1}^{\infty} \int \frac{d\mathbf{k}_1}{(2\pi)^3} \dots \int \frac{d\mathbf{k}_{n-1}}{(2\pi)^3} \int d\mathbf{k}_n \delta^D(\mathbf{k} - \mathbf{k}_1 - \dots - \mathbf{k}_n) Z_n(\mathbf{k}_1, \dots, \mathbf{k}_n) \delta_G(\mathbf{k}_1) \dots \delta_G(\mathbf{k}_n) \quad (3.10)$$

where the redshift space kernels $Z_n(\mathbf{k}_1, \dots, \mathbf{k}_n)$ are, up to second order

$$\begin{aligned} Z_1 &= b_{10} \underbrace{(1 + \beta\mu^2)}_{\text{Kaiser}} + \underbrace{\frac{b_{01}}{nG1}}_{\alpha} \quad (3.11) \\ Z_2 &= b_{10} \left[\underbrace{F_2(\mathbf{k}_1, \mathbf{k}_2)}_{\text{SQ1}} + f_{\text{NL}} \frac{\alpha(k)}{\alpha(k_1)\alpha(k_2)} \right] + \left[\underbrace{b_{20} - \frac{2}{7} b_{10}^L S_2(\mathbf{k}_1, \mathbf{k}_2)}_{\text{NLB}} \right] \\ &+ \underbrace{\frac{b_{11}}{2} \left[\frac{1}{\alpha(k_1)} + \frac{1}{\alpha(k_2)} \right] + \frac{b_{02}}{\alpha(k_1)\alpha(k_2)} - b_{01} \left[\frac{N_2(\mathbf{k}_1, \mathbf{k}_2)}{\alpha(k_2)} + \frac{N_2(\mathbf{k}_2, \mathbf{k}_1)}{\alpha(k_1)} \right]}_{\text{nG2}} + \\ &+ f\mu^2 \left[\underbrace{G_2(\mathbf{k}_1, \mathbf{k}_2)}_{\text{SQ2}} + f_{\text{NL}} \frac{\alpha(k)}{\alpha(k_1)\alpha(k_2)} \right] + \underbrace{\frac{f^2 k^2 \mu^2}{2} \frac{\mu_1 \mu_2}{k_1 k_2} + b_{10} \frac{f\mu k}{2} \left(\frac{\mu_1}{k_1} + \frac{\mu_2}{k_2} \right)}_{\text{FOG}} + \\ &+ \underbrace{b_{01} \frac{f\mu k}{2} \left[\frac{\mu_1}{k_1 \alpha(k_2)} + \frac{\mu_2}{k_2 \alpha(k_1)} \right]}_{\text{FoGnG}}, \quad (3.12) \end{aligned}$$

with $\mu_i \equiv \hat{k}_i \cdot \hat{z} = \mathbf{k}_i \cdot \hat{z} / k_i$. These kernels Z_i are important since they allow us to express the tree-level galaxy power spectrum and bispectrum in redshift space, by replacing $E_{1(2)} \rightarrow Z_{1(2)}$ in eqs. (2.31) and (2.32):

$$P_{gg}^s(\mathbf{k}_1) = Z_1^2(\mathbf{k}_1) P(k_1) \quad (3.13)$$

$$B_{ggg}^s(\mathbf{k}_1, \mathbf{k}_2, \mathbf{k}_3) = 2Z_1(\mathbf{k}_1) Z_1(\mathbf{k}_2) Z_2(\mathbf{k}_1, \mathbf{k}_2) P(k_1) P(k_2) + 2 \text{ cyc.}, \quad (3.14)$$

including the effects of PNG. The resulting expression for B_{ggg}^s – whose physics we will discuss more in detail in the next section – represents one of the main results of this paper². At this stage we

²A common factor $\mathcal{D}_{\text{FoG}}^B(k_1, k_2, k_3, \sigma_{\text{FoG}}^B[z])$ is usually included in the r.h.s of eq. (3.14), accounting for the FoG damping due to intra-cluster velocity dispersion, beyond linear level [93]. This phenomenological extension, which describes N-body data, will not be considered here for the purpose of getting an analytic result in the next section.

can make some considerations with respect to the various contributions to the Z_i , which we will then develop in what comes next.

Considering Z_1 , it contains the bias b_{10} and the scale-dependent correction (nG1). At linear level, RSD introduce the quantity $\beta\mu^2 \geq 0$, explaining why objects are more clustered in redshift space (compared to real space). The term $(1 + \beta\mu^2)$ is often referred to as the ‘Kaiser factor’ [50], where $\beta = f/b_{10}$ and is regularly accounted for in studies of galaxy clustering (e.g. [94]).

For Z_2 , we notice that the contributions that we label with SQ1 (linear squashing), NLB (non-linear bias), nG2 (second order non Gaussian effects) are already present in the expressions for E_2 (eq. (2.34)) controlling the bispectrum in real space. On the other hand, the remaining three contributions are generated by redshift-space distortions. The quantities SQ2 (second order squashing) and FOG are already well studied in the literature.

Interestingly, we notice the presence of a qualitatively new term (FoGnG), induced by PNG. It mimics the FOG contribution, *but* with an amplification of $1/\alpha(k)$. In a sense, it is an analogue for RSD of the scale-dependent bias of the galaxy power spectrum induced by PNG. The FoGnG term is sourced by the coupling between u_z and φ_G (first integrand in eq. (3.9)), potentially affecting large-scale measurements. Therefore, neglecting it would introduce a systematic error, resulting in a biased f_{NL} measurement from the tree-level of the bispectrum³.

As pointed out in [59], the galaxy overdensity of eq. (3.10) is the result of two approximations: one is the power series expansion (eq. (3.2)) of the redshift space mapping (eq. (3.1)), the other one is the perturbative expansion of $\delta(\mathbf{k})$ and $\theta(\mathbf{k})$ (eqs. (2.1) and (2.2)). Therefore, the perturbation theory in redshift space is expected to break down on larger scales than in real space. However, replacing the kernels with effective kernels calibrated against simulations can extend the validity of the results based on eq. (3.10), as shown in [95]. Although we will not implement these techniques here, the replacement is straightforward.

3.2 Galaxy bispectrum monopole

In this section, we choose to investigate the galaxy bispectrum monopole, i.e. the angle averaged bispectrum along the direction of the line of sight. The reason is to extend the monopole model used in the recent measurement by Gil-Marín et al. [52, 95, 96] to the case of PNG. The result of this section can thus be applied in a similar analysis, aiming to measure f_{NL} .

The galaxy bispectrum in redshift space is a function of five variables: three of them (say k_1, k_2 and $\hat{k}_1 \cdot \hat{k}_2 = \cos\theta_{12}$) fully define the shape of the triangle, while the polar angle $\omega = \arccos\mu_1$ and the azimuthal angle ϕ about \hat{k}_1 describe how it is oriented with respect to the line of sight. All the angles between the vectors $\mathbf{k}_1, \mathbf{k}_2, \mathbf{k}_3$ and the line of sight \hat{z} can be written in terms of μ_1 and ϕ [93]:

$$\mu_1 = \cos\omega = \hat{k}_1 \cdot \hat{z}, \quad \mu_2 = \mu_1 \cos\theta_{12} - \sqrt{(1 - \mu_1^2)} \sin\theta_{12} \cos\phi, \quad \mu_3 = -\frac{k_1}{k_3}\mu_1 - \frac{k_2}{k_3}\mu_2. \quad (3.15)$$

The (μ_1, ϕ) -dependence introduced by redshift space distortions can be conveniently decomposed into spherical harmonics,

$$B_{ggg}^s(\mathbf{k}_1, \mathbf{k}_2, \omega, \phi) = \sum_{l=0}^{\infty} \sum_{m=-l}^l B_{ggg}^{s(l,m)}(\mathbf{k}_1, \mathbf{k}_2) Y_{lm}(\omega, \phi). \quad (3.16)$$

As we mentioned, we focus only on the monopole ($l=0, m=0$), i.e. the average over all the possible orientations of the bispectrum with respect to the line of sight,

$$B_{ggg}^{s(0,0)}(\mathbf{k}_1, \mathbf{k}_2) = \frac{1}{4\pi} \int_{-1}^{+1} d\mu_1 \int_0^{2\pi} d\phi B_{ggg}^s(\mathbf{k}_1, \mathbf{k}_2, \omega, \phi), \quad (3.17)$$

although the large-scale enhancement of PNG in redshift space, associated with the term called FoGnG (see eq. (3.12)), is found also in higher multipoles, since it is not cancelled by angular integrations.

³At the power spectrum level, the FoGnG term enters as a loop correction. However, we do not consider its consequences in this paper, since we only focus on large scale effects.

We start by quoting the monopole for Gaussian initial conditions ($f_{\text{NL}} = 0$) [93, 95]

$$B_{ggg}^{sG(0,0)}(\mathbf{k}_1, \mathbf{k}_2) = b_{10}^4 \left\{ \frac{1}{b_{10}} \mathcal{F}_2(\mathbf{k}_1, \mathbf{k}_2) \mathcal{D}_{\text{SQ1}} + \frac{1}{b_{10}} \mathcal{G}_2(\mathbf{k}_1, \mathbf{k}_2) \mathcal{D}_{\text{SQ2}} + \left[\frac{b_{20}}{b_{10}^2} - \frac{2}{7} \frac{b_{10}^L}{b_{10}^2} \mathcal{S}_2(\mathbf{k}_1, \mathbf{k}_2) \right] \mathcal{D}_{\text{NLB}} + \mathcal{D}_{\text{FOG}} \right\} P(k_1) P(k_2) + 2 \text{ cyc.} . \quad (3.18)$$

The terms \mathcal{D}_{SQ1} and \mathcal{D}_{SQ2} represent the linear and non-linear contributions to the large-scale squashing, \mathcal{D}_{NLB} the non-linear bias contribution and, finally, \mathcal{D}_{FOG} accounts for the linear part of FoG, i.e. the damping effect due to velocity dispersion. The labelling that we introduced in eqs. (3.11) and (3.12) helps to understand where these factors come from: schematically \mathcal{D}_{SQ1} is the result of the angular average of the Kaiser factor squared times the term SQ1, \mathcal{D}_{SQ2} of the Kaiser factor squared times SQ2 and so on. Appendix C further clarifies these points, with explicit expressions for the \mathcal{D} -factors. Here and after we omit their explicit dependence $\mathcal{D}(k_i, k_j, \cos \theta_{ij}, y_{ij}, \beta)$ to simplify the notation, but they are among the quantities to be permuted.

We now generalise the previous result to the case of local-type PNG; it can be written as

$$B_{ggg}^{s(0,0)}(\mathbf{k}_1, \mathbf{k}_2) = b_{10}^4 \left\{ \frac{1}{b_{10}} \left[\mathcal{F}_2(\mathbf{k}_1, \mathbf{k}_2) + f_{\text{NL}} \frac{\alpha(k_3)}{\alpha(k_1)\alpha(k_2)} \right] \mathcal{D}_{\text{SQ1}} \mathcal{R}_{\text{SQ1}} + \frac{1}{b_{10}} \left[\mathcal{G}_2(\mathbf{k}_1, \mathbf{k}_2) + f_{\text{NL}} \frac{\alpha(k_3)}{\alpha(k_1)\alpha(k_2)} \right] \mathcal{D}_{\text{SQ2}} \mathcal{R}_{\text{SQ2}} + \left[\frac{b_{20}}{b_{10}^2} - \frac{2}{7} \frac{b_{10}^L}{b_{10}^2} \mathcal{S}_2(\mathbf{k}_1, \mathbf{k}_2) \right] \mathcal{D}_{\text{NLB}} \mathcal{R}_{\text{NLB}} + \mathcal{D}_{\text{FOG}} \mathcal{R}_{\text{FOG}} + \frac{1}{b_{10}^2} \left[\frac{b_{11}}{2} \left(\frac{1}{\alpha(k_1)} + \frac{1}{\alpha(k_2)} \right) - b_{01} \left(\frac{\mathcal{N}_2(\mathbf{k}_1, \mathbf{k}_2)}{\alpha(k_2)} + \frac{\mathcal{N}_2(\mathbf{k}_2, \mathbf{k}_1)}{\alpha(k_1)} \right) + \frac{b_{02}}{\alpha(k_1)\alpha(k_2)} \right] \times \mathcal{D}_{\text{nG2}} \mathcal{R}_{\text{nG2}} + \frac{b_{01}}{b_{10}} \mathcal{D}_{\text{FoGnG}} \mathcal{R}_{\text{FoGnG}} \right\} P(k_1) P(k_2) + 2 \text{ cyc.} , \quad (3.19)$$

where we have introduced the correction factors

$$\mathcal{R}_{\text{SQ1}} = 1 + \frac{1}{\mathcal{D}_{\text{SQ1}}} \left(\frac{b_{01}^2}{b_{10}^2} \frac{2}{\alpha(k_1)\alpha(k_2)} + \frac{b_{01}}{b_{10}} \mathcal{D}_{\text{SQ1}}^{\text{nG1}} \right) \quad (3.20)$$

$$\mathcal{R}_{\text{SQ2}} = 1 + \frac{1}{\mathcal{D}_{\text{SQ2}}} \left(\frac{b_{01}}{b_{10}} \mathcal{D}_{\text{SQ2}}^{\text{nG1}} + \frac{b_{01}^2}{b_{10}^2} \mathcal{D}_{\text{SQ2}}^{\text{nG1}^2} \right) \quad (3.21)$$

$$\mathcal{R}_{\text{NLB}} = 1 + \frac{1}{\mathcal{D}_{\text{NLB}}} \left(\frac{b_{01}^2}{b_{10}^2} \frac{2}{\alpha(k_1)\alpha(k_2)} + \frac{b_{01}}{b_{10}} \mathcal{D}_{\text{NLB}}^{\text{nG1}} \right) \quad (3.22)$$

$$\mathcal{R}_{\text{FOG}} = 1 + \frac{1}{\mathcal{D}_{\text{FOG}}} \left(\frac{b_{01}}{b_{10}} \mathcal{D}_{\text{FOG}}^{\text{nG1}} + \frac{b_{01}^2}{b_{10}^2} \mathcal{D}_{\text{FOG}}^{\text{nG1}^2} \right) \quad (3.23)$$

$$\mathcal{R}_{\text{nG2}} = 1 + \frac{1}{\mathcal{D}_{\text{nG2}}} \left(\frac{b_{01}^2}{b_{10}^2} \frac{2}{\alpha(k_1)\alpha(k_2)} + \frac{b_{01}}{b_{10}} \mathcal{D}_{\text{nG2}}^{\text{nG1}} \right) \quad (3.24)$$

$$\mathcal{R}_{\text{FoGnG}} = 1 + \frac{1}{\mathcal{D}_{\text{FoGnG}}} \left(\frac{b_{01}}{b_{10}} \mathcal{D}_{\text{FoGnG}}^{\text{nG1}} + \frac{b_{01}^2}{b_{10}^2} \mathcal{D}_{\text{FoGnG}}^{\text{nG1}^2} \right) . \quad (3.25)$$

We see that PNG enters into the expression (3.19) in four different ways:

- The kernels \mathcal{F}_2 and \mathcal{G}_2 acquire a correction proportional to f_{NL} , as seen in section 2.1.
- The linear (SQ1) and non-linear (SQ2) squashing, non-linear biasing (NLB) and linear part of FoG (FOG) are modified by the correction factors \mathcal{R}_{SQ1} , \mathcal{R}_{SQ2} , \mathcal{R}_{NLB} and \mathcal{R}_{FOG} , respectively. In these, for instance, $\mathcal{D}_{\text{SQ1}}^{\text{nG1}}$ comes from the angular average of the Kaiser factor times SQ1 times nG1 (linear effect of PNG), $\mathcal{D}_{\text{NLB}}^{\text{nG1}}$ from the Kaiser factor times NLB time nG1, $\mathcal{D}_{\text{SQ2}}^{\text{nG1}^2}$ from the SQ2 term times nG1 squared, and so on.

- Non-Gaussianity distortions appear in the non-linear effect of PNG through the term $\mathcal{D}_{\text{nG2}}\mathcal{R}_{\text{nG2}}$. In particular, \mathcal{D}_{nG2} is generated by the integration of the Kaiser factor squared times the non-linear effect of PNG (nG2) and $\mathcal{D}_{\text{nG2}}^{\text{nG1}}$ by the angular average of the Kaiser factor times nG1 times nG2.
- Importantly, a new set of terms appear, potentially relevant at large scales, related to the quantity called FoGnG in eq. (3.12). $\mathcal{D}_{\text{FoGnG}}$ is the result of the integration of the Kaiser factor squared times FoGnG, $\mathcal{D}_{\text{FoGnG}}^{\text{nG1}}$ of the Kaiser factor times FoGnG times nG1 and, finally, $\mathcal{D}_{\text{FoGnG}}^{\text{nG1}^2}$ by the angular average of the FoGnG term times nG1 squared.

Appendix C further discusses in detail all the \mathcal{D} -factors that we schematically described here.

In order to provide an illustration of the role played by PNG in redshift space, we plot in fig. 1 the absolute value of the relative difference between the non-Gaussian and the Gaussian monopole,

$$\text{Diff}(\mathbf{k}_1, \mathbf{k}_2, \mathbf{k}_3) = \left| \frac{B_{ggg}^s(0,0) - B_{ggg}^{sG}(0,0)}{B_{ggg}^{sG}(0,0)} \right|, \quad (3.26)$$

assuming $f_{\text{NL}} = 10$ and objects with mass $M = 10^{13}h^{-1}M_{\odot}$. The plots are based on the graphical representation of [37], i.e. the amplitude of the signal is presented in a colour map as a function of k_2/k_1 and k_3/k_1 , under the condition $k_3 \leq k_2 \leq k_1$, which avoids multiple visualizations of the same triangle/configuration.

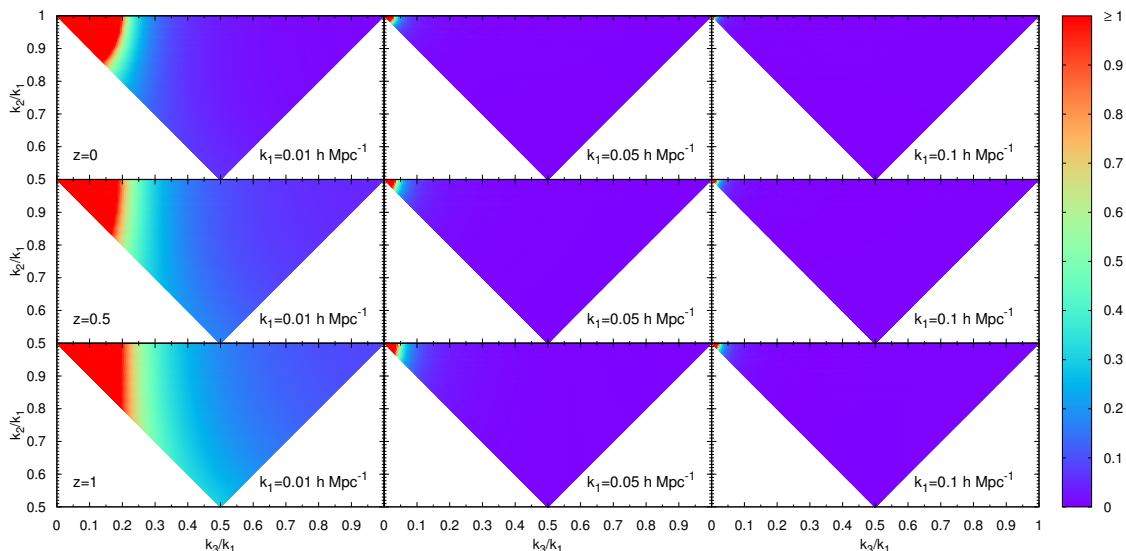


Figure 1: The plots show the absolute value of the relative difference between the galaxy bispectrum monopole with PNG and the one without, for objects with mass $M = 10^{13}h^{-1}M_{\odot}$ and $f_{\text{NL}} = 10$. The colour maps display the amplitude of the signal as a function of k_2/k_1 and k_3/k_1 , under the condition $k_3 \leq k_2 \leq k_1$. Differences above 100% are saturated to the same red colour of the palette.

The primordial non-Gaussian signal clearly peaks in the squeezed limit (top left corners) of the galaxy monopole, mainly on large scales and/or high redshift. On the other hand, interestingly, a non-negligible signal propagates also into other configurations, with decreasing amplitude as it approaches the equilateral configuration (top right corners). We interpret this effect, at least partly, as due to the new contributions FoGnG discussed above; primordial non-Gaussianity in redshift space induces distortions that can affect large scale measurements. Failing to include all the non-Gaussian effects together with RSD would result into biased measurements of f_{NL} .

4 Fisher Analysis

As the recent measurement of Gil-Marín *et al* [52, 96] shows, the bispectrum is a valuable tool for cosmology. In particular, the larger amount of available configurations in a wavelength range between k_{\min} and k_{\max} compared to the power spectrum may well shrink the observational bounds on f_{NL} even further, as many works show [33–35, 97], potentially below the *Planck* constraint [98]. The monopole derived in the previous section naturally extends the model considered by Gil-Marín *et al* [95] to the case of local-type PNG and can be used to measure f_{NL} .

However, it may not be the only way to improve our constraints on inflation: the multi-tracer technique is a promising tool [27]. Even the novel position-dependent power spectrum could be an interesting alternative, although a detailed analysis in the case of PNG is still missing (see the discussion in appendix B). As both involve measurements of the power spectrum, they require less efforts than a full bispectrum analysis.

In this section we present forecasts of the accuracy in determining f_{NL} – a quantity that we call $\sigma_{f_{\text{NL}}}$ – based on a Fisher analysis for the bispectrum. Our aim is to give an illustration of the best possible improvement one could get with respect to power spectrum forecasts, when a single tracer is considered [24, 57]. On the other hand, important effects (like the covariance between different triangles) will be neglected and the quoted results are by no means intended to be fully realistic; rather, they are meant to motivate future work. For this reason we will consider only the bispectrum in real space, which is computationally easier to handle than the redshift space result. Although forecasts based on the redshift-space bispectrum can have some small quantitative differences respect to our results, we expect the following qualitative discussion to hold anyway⁴.

The Fisher formalism is a tool for setting a lower limit on the statistical uncertainties that future surveys will have in the measurements of cosmological parameters of interest (see [99–101] for an introduction). The Fisher matrix information is defined as

$$F_{\alpha\beta} \equiv - \left\langle \frac{\partial^2 \ln L(\mathbf{x}; p)}{\partial p_\alpha \partial p_\beta} \right\rangle, \quad (4.1)$$

where $L(\mathbf{x}; p)$ is the likelihood function, i.e the probability of the data \mathbf{x} given the parameters p , and p_α is the α -th unknown parameter. If all the parameters are fixed except one (say p_α), then the lower limit on the 1σ error bar in the p_α measurement is $\sigma_{p_\alpha} = 1/\sqrt{F_{\alpha\alpha}}$. Otherwise, if we marginalise over the parameters, the lower bound becomes $\sigma_{p_\alpha} = \sqrt{F_{\alpha\alpha}^{-1}}$.

The Fisher matrix for the bispectrum is [33, 98]

$$F_{\alpha\beta} \equiv \sum_z \sum_{k_1, k_2, k_3 \geq k_{\min}}^{k_{\max}} \frac{1}{\Delta B^2(k_1, k_2, k_3)} \frac{\partial B(k_1, k_2, k_3)}{\partial p_\alpha} \frac{\partial B(k_1, k_2, k_3)}{\partial p_\beta} \quad (4.2)$$

where B and ΔB^2 are the bispectrum and covariance estimator respectively and we assume the minimum value of k to be fixed by the survey volume V , $k_{\min} = 2\pi/V^{1/3}$, while the maximum is $k_{\max} = 0.1D(0)/D(z)$ – a reasonable limit for the validity of the non-linear analytic model [57].

4.1 Methodology

To compute the Fisher matrix we need to define B , ΔB^2 and the set of unknown parameters p ; our assumptions are described below.

⁴Technically, studies on the cumulative signal-to-noise, i.e. summed over all the configurations, show the critical dependence of the halo bispectrum signal on some kind of triangle configurations and the maximum wavenumber, k_{\max} , considered [35, 97]. At large scales ($k_{\max} < 0.05h\text{Mpc}^{-1}$), the signal is strongly suppressed because only few configurations are available, and with a large variance. By increasing k_{\max} , the number of triangles considerably grows ($N_{\text{Tr}} \sim k_{\max}^3$) and, consequently, the signal. As fig. 1 suggests, a large fraction of it is in squeezed configurations. Among these, the FoGnG term can play a role on those that have their smallest k on sufficiently large scales. However, one should bear in mind that these large-scale, squeezed triangles are highly correlated, i.e. the covariance cannot be neglected (see also the discussion in section 4.1). Thus, we expect that forecasts based on the redshift-space bispectrum will have small differences respect to our results, but it is clear that failing to include RSD in the bispectrum model could bias a f_{NL} measurement at the level of accuracy that is now required.

We assume the bispectrum model of eq. (2.32), while the covariance for a survey of volume V is given by [102]

$$(\Delta B)^2 = s_{123} \frac{V_f}{V_{123}} \left(P_{gg}(k_1) + \frac{1}{\bar{n}} \right) \left(P_{gg}(k_2) + \frac{1}{\bar{n}} \right) \left(P_{gg}(k_3) + \frac{1}{\bar{n}} \right), \quad (4.3)$$

where the volume of the fundamental cell is $V_f = (2\pi)^3/V$ and $V_{123} \approx 8\pi^2 k_1 k_2 k_3 \delta k^3$, with δk being the bin size. \bar{n} is the number density of objects accounting for the shot noise, while s_{123} is the symmetry factor, respectively $s_{123} = 6, 2, 1$ for equilateral, isosceles and general configurations. In the noise estimator, the power spectrum is approximated by the leading contribution $P_{gg}(k) = (b_{10} + b_{01}/\alpha(k))^2 P(k)$.

For simplicity and as in other studies [33–35, 97, 103], we neglect the covariance between different configurations of the bispectrum which is expected to be non-negligible for triangles sharing one or two sides, in particular on large scales [104]. The induced covariance arising from survey selection effects (i.e. complicated survey geometry and mask) is ignored as well.

As explained in [34], the results of [33] suggest that ignoring covariance can over-estimate the constraining power of a given sample by a factor of two for $k < 0.1 h\text{Mpc}^{-1}$ and up to a factor of eight for $k < 0.3 h\text{Mpc}^{-1}$ at redshift zero. At higher redshift the contribution from a connected 6-point function generated by non-linear gravitational evolution is expected to be less important and thus the (theoretical) covariance reduced. The largest k values used in our forecasts lie between $0.15 h\text{Mpc}^{-1}$ and $0.25 h\text{Mpc}^{-1}$ in the redshift range $0 < z < 2.2$; suggesting covariance could make our forecasts optimistic by a factor of ~ 5 . However, we will show that the constraining power in current and future surveys would provide competitive f_{NL} constraints even if the covariance degrades our idealised forecasts by a factor of 5, although a more realistic analysis is needed to fully explore this.

We assume all the cosmological parameters to be fixed to *Planck*'s central values [105], except for the linear and non-linear bias and f_{NL} , thus $p = \{b_{10}, b_{20}, f_{\text{NL}}\}$. The fiducial model that maximizes the likelihood is assumed to be $p = \{b_{10}^{\text{fid}}, b_{20}^{\text{fid}}, f_{\text{NL}}^{\text{fid}} = 0\}$, where b_{10}^{fid} is calibrated against real data (either from the particular survey or characteristic of the type of galaxy expected to be observed by the particular survey) and will be quoted in the following paragraphs, depending on the survey and the tracer. $f_{\text{NL}}^{\text{fid}}$ is assumed to be vanishing, this being compatible with current data: the final results will give an idea of the significance level at which a non-null primordial signal can be detected.

Since the non-linear bias is not a well constrained parameter, the choice of the fiducial value is very important. We take it to be the analytic prediction $b_{20}^{\text{fid}} = b_{20}(\nu)$, based on eqs. (2.25), (A.10) and (A.11), where the variable ν is estimated under the assumption $b_{10}(\nu) = b_{10}^{\text{fid}}$. We will then show how much $\sigma_{f_{\text{NL}}}$ is affected by the choice of b_{20}^{fid} by allowing for a ± 1 range around this value. Therefore, the results are presented in table 1 in the following form:

$$\sigma_{f_{\text{NL}}, b_{20}^{\text{fid}}} \left(\begin{array}{c} \sigma_{f_{\text{NL}}, b_{20}^{\text{fid}}+1} \\ \sigma_{f_{\text{NL}}, b_{20}^{\text{fid}}-1} \end{array} \right).$$

In our analysis we consider four redshift surveys: BOSS, eBOSS, DESI and Euclid, briefly presented below. The data used for each of them can be found in the tables in appendix D.

BOSS

SDSS-III's Baryon Oscillation Spectroscopic Survey [53] is a galaxy redshift survey, which finished observations in 2014. It mapped the spatial distribution of about 1.5 million luminous red galaxies (LRGs)⁵, covering $10,000 \text{ deg}^2$ in the redshift range $0 < z < 0.8$, with the primary goal of detecting the characteristic scale imprinted by sound waves in the early universe, i.e. the Baryon Acoustic Oscillations (BAO). Also, about 160,000 quasars (QSOs) were observed in the redshift range $2.2 < z < 3$, so that correlations can be measured in the Lyman- α forest, which we will not consider here. Table 2 in appendix D shows the basic numbers for BOSS, with the linear bias assumed to be $b_{10}^{\text{LRG}} = 1.7/D(z)$ (see [24] and references therein).

⁵Strictly speaking, BOSS also contains a sample of luminous galaxies with more star formation and greater disk morphology than typical LRGs.

eBOSS

The extended Baryon Oscillation Spectroscopic Survey [54] is part of the SDSS-IV project and started observations in 2014. It will extend the BAO measurements to $0.6 < z < 2.2$ by observing LRGs, Emission Line Galaxies (ELGs) and QSOs.

The eBOSS numbers we use match those presented in [57]. LRGs will be observed in the redshift range $0.6 < z < 1$ over $7,000 \text{ deg}^2$, with a linear bias assumed to be $b_{10}^{\text{LRG}} = 1.7/D(z)$, while QSOs will fall in the range $0.6 < z < 2.2$ over $7,500 \text{ deg}^2$, with bias $b_{10}^{\text{QSO}} = 0.53 + 0.29(1+z)^2$. The ELG target selection definitions have not been finalised, but each of the three proposals considered in [57] result in samples that have a significant overlap in volume with the LRG sample. We have tested each potential ELG sample and found that even if they are treated independently, they do not add substantial constraining power. Therefore, we omit them from the forecast constraints we present. Tables 3 to 5 show the basic numbers for eBOSS LRGs, QSOs and ELGs respectively. Refer to [57] and references therein for further details.

DESI

Dark Energy Spectroscopic Instrument [55] is a redshift survey with the primary target of measuring the effect of dark energy on the expansion of the Universe. It is expected to run between 2018 and 2022 and will map the universe from low to high redshift over $14,000 \text{ deg}^2$, measuring the optical spectra for tens of million objects, including LRGs, ELGs and QSOs.

The LRGs will fall in the redshift range $0.1 < z < 1.1$ with a linear bias assumed to be $b_{10}^{\text{LRG}} = 1.7/D(z)$, ELGs in $0.1 < z < 1.8$ with $b_{10}^{\text{ELG}} = 0.84/D(z)$ and QSOs will be considered in redshift range $0.1 < z < 1.9$, with bias $b_{10}^{\text{QSO}} = 1.2/D(z)$. Table 6 shows the basic numbers for DESI (see [24] and references therein).

Euclid

Euclid [56] is a space mission developed to study the imprints of dark energy and gravity. The expansion rate of the Universe and the growth of structures will be tracked by using two complementary observables: weak gravitational lensing and galaxy clustering. Its launch is planned for 2020.

We focus on the redshift survey part of the mission, which is expected to detect about 50 million galaxies in the redshift range $0.6 < z < 2.1$, over $15,000 \text{ deg}^2$. The fiducial value for the bias is assumed to be $b_{10} = 0.76/D(z)$. Table 7 shows the basic numbers for Euclid (see [24] and references therein).

4.2 Results

Given the assumptions listed above, table 1 shows the lower limit on $\sigma_{f_{\text{NL}}}$ that could be expected from the bispectrum of BOSS, eBOSS, DESI and Euclid. We also present the forecast results for the power spectrum, in order to provide a comparison. The results combine all the tracers available for each survey (LRGs, ELGs, QSOs), which are treated as independent, except that we omit any ELG sample for eBOSS, as previously noted.

If we focus first on the results labelled ‘bias float’ (marginalising over bias) of the bispectrum set of columns, our analysis suggests that BOSS and eBOSS will both be able to reach $\sigma_{f_{\text{NL}}} \simeq 1$. eBOSS appears to be penalised compared to BOSS because of the lower number densities. Interestingly, DESI and Euclid may give $\sigma_{f_{\text{NL}}} < 1$, regardless of the chosen fiducial value for b_{20} , within ± 1 range. The DESI result is more stringent than the Euclid one because DESI is assumed to observe more biased objects; however, combining the BOSS and Euclid data tighten the constraint towards the DESI result. Clearly, the f_{NL} measurements improve by fixing the linear and non-linear bias: the results on the last column (bias fixed) of table 1 indicate an improvement factor between 1.4 and 2 on $\sigma_{f_{\text{NL}}}$.

A comparison between $\sigma_{f_{\text{NL}}}$ expected from the bispectrum and those from the power spectrum of a single tracer (first two columns of table 1, but see also [24, 57]) seems to indicate about an order of magnitude improvement. Even allowing for a factor of five dilution in constraining power potentially caused by covariance between triangle configurations, our forecasts remain impressive. Indeed, we forecast that current BOSS data should allow f_{NL} constraints competitive with those obtained from *Planck* [8].

Table 1: Forecasts for $\sigma_{f_{\text{NL}}}$ from the bispectrum of BOSS, eBOSS, DESI and Euclid, assuming the fiducial values $p = \{b_{10}^{\text{fid}}, b_{20}^{\text{fid}}, f_{\text{NL}}^{\text{fid}} = 0\}$, as described in section 4.1. Forecasts from the power spectrum are obtained considering only the tree-level, with the fiducial model $p = \{b_{10}^{\text{fid}}, f_{\text{NL}}^{\text{fid}} = 0\}$. The results with marginalisation over the bias factors are shown on the left columns (bias float), while those without on the right (bias fixed). The numbers inside the parenthesis in the superscripts are the predictions for $\sigma_{f_{\text{NL}}}$ considering the fiducial value for the non-linear bias to be $b_{20}^{\text{fid}} + 1$, while those in the subscripts assume $b_{20}^{\text{fid}} - 1$.

Sample	Power Spectrum		Bispectrum	
	$\sigma_{f_{\text{NL}}}$ bias float	$\sigma_{f_{\text{NL}}}$ bias fixed	$\sigma_{f_{\text{NL}}}$ bias float	$\sigma_{f_{\text{NL}}}$ bias fixed
BOSS	21.30	13.28	1.04 ^(0.65) _(2.47)	0.57 ^(0.35) _(1.48)
eBOSS	14.21	11.12	1.18 ^(0.82) _(2.02)	0.70 ^(0.48) _(1.29)
Euclid	6.00	4.71	0.45 ^(0.18) _(0.71)	0.32 ^(0.12) _(0.35)
DESI	5.43	4.37	0.31 ^(0.17) _(0.48)	0.21 ^(0.12) _(0.37)
BOSS + Euclid	5.64	4.44	0.39 ^(0.17) _(0.59)	0.28 ^(0.11) _(0.34)

5 Conclusions

The target sensitivity of $f_{\text{NL}} \sim 1$ sets a new challenge in the search for primordial non-Gaussianity. While future CMB experiments may not be able to achieve this goal, large-scale structure observations hold the promise to reach this level of sensitivity, by exploiting the characteristic scale-dependence introduced by local-type models in the bias relation between collapsed objects and the density field, and the very large amount of data available with future redshift surveys.

In this work, we have studied the sensitivity of galaxy bispectrum measurements to f_{NL} , tackling the problem from two separate directions. We first addressed the problem of modelling redshift space distortions in the tree-level galaxy bispectrum with primordial non-Gaussianity of local-type. We examined how redshift space distortions can affect large-scale measurements, and therefore potentially lead to a biased measurement of f_{NL} if not properly described. In particular, we identified new contributions to the galaxy bispectrum, which physically correspond to large-scale amplifications – induced by primordial non-Gaussianity – of redshift space distortion effects. Moreover, we proposed an analytic prediction for the monopole which can be used to fit against data, in the large scale regimes where the non-linear part of FoG can be neglected. We analysed the physical consequences of our findings, providing a graphical method for comparing our results for bispectra with the case in which primordial non-Gaussianity is not included.

We then performed idealised forecasts of $\sigma_{f_{\text{NL}}}$, the accuracy of the determination of local f_{NL} , that could be obtained from measurements of the galaxy bispectrum using data from surveys like BOSS, eBOSS, DESI and Euclid. Our findings suggest that the bispectrum of galaxies in current and future surveys will provide competitive f_{NL} constraints even if the covariance between triangle configurations degrades our idealised forecasts by a factor of 5. In particular, current BOSS data should allow for *Planck*-like constraints on f_{NL} , while future surveys like Euclid and DESI will contain the statistical power to shrink the bound by an additional factor of three.

We leave as a challenge for future work to obtain improved predictions for $\sigma_{f_{\text{NL}}}$ fully accounting for the covariance: this will be necessary if we are to completely understand the power of bispectrum measurements to constrain f_{NL} compared to alternative approaches, such as the multi-tracer technique or the position-dependent power spectrum.

Acknowledgments

MT wishes to thank Héctor Gil-Marín, Yuting Wang, Benedict Kalus, Davide Bianchi and Gong-Bo Zhao for many helpful discussions on the topics of redshift space distortions and Fisher analysis. He also acknowledges Marco Crisostomi, for help with *Mathematica* and sharing his enthusiasm, and

Donough Regan for providing useful comments. GT is supported by STFC grant ST/N001435/1. DW is supported by STFC grants ST/K00090X/1 and ST/L005573/1.

References

- [1] A. R. Liddle and D. H. Lyth, *Cosmological inflation and large scale structure*. 2000.
- [2] N. Bartolo, E. Komatsu, S. Matarrese and A. Riotto, *Non-Gaussianity from inflation: Theory and observations*, *Phys.Rept.* **402** (2004) 103–266, [[astro-ph/0406398](#)].
- [3] A. Gangui, F. Lucchin, S. Matarrese and S. Mollerach, *The Three point correlation function of the cosmic microwave background in inflationary models*, *Astrophys.J.* **430** (1994) 447–457, [[astro-ph/9312033](#)].
- [4] L. Verde, L.-M. Wang, A. Heavens and M. Kamionkowski, *Large scale structure, the cosmic microwave background, and primordial non-gaussianity*, *Mon.Not.Roy.Astron.Soc.* **313** (2000) L141–L147, [[astro-ph/9906301](#)].
- [5] E. Komatsu and D. N. Spergel, *Acoustic signatures in the primary microwave background bispectrum*, *Phys.Rev.* **D63** (2001) 063002, [[astro-ph/0005036](#)].
- [6] B. A. Bassett, S. Tsujikawa and D. Wands, *Inflation dynamics and reheating*, *Rev. Mod. Phys.* **78** (2006) 537–589, [[astro-ph/0507632](#)].
- [7] J. M. Maldacena, *Non-Gaussian features of primordial fluctuations in single field inflationary models*, *JHEP* **05** (2003) 013, [[astro-ph/0210603](#)].
- [8] PLANCK collaboration, P. Ade et al., *Planck 2015 results. XVII. Constraints on primordial non-Gaussianity*, **1502.01592**.
- [9] M. Alvarez, T. Baldauf, J. R. Bond, N. Dalal, R. de Putter et al., *Testing Inflation with Large Scale Structure: Connecting Hopes with Reality*, **1412.4671**.
- [10] N. Dalal, O. Dore, D. Huterer and A. Shirokov, *The imprints of primordial non-gaussianities on large-scale structure: scale dependent bias and abundance of virialized objects*, *Phys.Rev.* **D77** (2008) 123514, [[0710.4560](#)].
- [11] S. Matarrese and L. Verde, *The effect of primordial non-Gaussianity on halo bias*, *Astrophys.J.* **677** (2008) L77–L80, [[0801.4826](#)].
- [12] A. Slosar, C. Hirata, U. Seljak, S. Ho and N. Padmanabhan, *Constraints on local primordial non-Gaussianity from large scale structure*, *JCAP* **0808** (2008) 031, [[0805.3580](#)].
- [13] N. Afshordi and A. J. Tolley, *Primordial non-gaussianity, statistics of collapsed objects, and the Integrated Sachs-Wolfe effect*, *Phys.Rev.* **D78** (2008) 123507, [[0806.1046](#)].
- [14] J.-Q. Xia, M. Viel, C. Baccigalupi, G. De Zotti, S. Matarrese and L. Verde, *Primordial Non-Gaussianity and the NRAO VLA Sky Survey*, *Astrophys. J. Let.* **717** (July, 2010) L17–L21, [[1003.3451](#)].
- [15] J.-Q. Xia, A. Bonaldi, C. Baccigalupi, G. De Zotti, S. Matarrese, L. Verde et al., *Constraining primordial non-Gaussianity with high-redshift probes*, *JCAP* **8** (Aug., 2010) 13, [[1007.1969](#)].
- [16] A. J. Ross, W. J. Percival, A. Carnero, G.-b. Zhao, M. Manera, A. Raccanelli et al., *The clustering of galaxies in the SDSS-III DR9 Baryon Oscillation Spectroscopic Survey: constraints on primordial non-Gaussianity*, *Mon. Not. Roy. Astron. Soc.* **428** (Jan., 2013) 1116–1127, [[1208.1491](#)].
- [17] D. Karagiannis, T. Shanks and N. P. Ross, *Search for primordial non-Gaussianity in the quasars of SDSS-III BOSS DR9*, *Mon.Not.Roy.Astron.Soc.* **441** (2014) 486–502, [[1310.6716](#)].
- [18] T. Giannantonio, A. J. Ross, W. J. Percival, R. Crittenden, D. Bacher et al., *Improved Primordial Non-Gaussianity Constraints from Measurements of Galaxy Clustering and the Integrated Sachs-Wolfe Effect*, *Phys.Rev.* **D89** (2014) 023511, [[1303.1349](#)].
- [19] S. Ho, N. Agarwal, A. D. Myers, R. Lyons, A. Disbrow et al., *Sloan Digital Sky Survey III Photometric Quasar Clustering: Probing the Initial Conditions of the Universe using the Largest Volume*, **1311.2597**.

- [20] T. Giannantonio and W. J. Percival, *Using correlations between CMB lensing and large-scale structure to measure primordial non-Gaussianity*, *Mon.Not.Roy.Astron.Soc.* **441** (2014) L16L20, [[1312.5154](#)].
- [21] B. Leistedt, H. V. Peiris and N. Roth, *Constraints on Primordial Non-Gaussianity from 800000 Photometric Quasars*, *Phys.Rev.Lett.* **113** (2014) 221301, [[1405.4315](#)].
- [22] C. L. Bennett, D. Larson, J. L. Weiland, N. Jarosik, G. Hinshaw, N. Odegard et al., *Nine-year Wilkinson Microwave Anisotropy Probe (WMAP) Observations: Final Maps and Results*, *Astrophys. J. Sup.* **208** (Oct., 2013) 20, [[1212.5225](#)].
- [23] T. Giannantonio, C. Porciani, J. Carron, A. Amara and A. Pillepich, *Constraining primordial non-Gaussianity with future galaxy surveys*, *Mon. Not. Roy. Astron. Soc.* **422** (June, 2012) 2854–2877, [[1109.0958](#)].
- [24] A. Font-Ribera, P. McDonald, N. Mostek, B. A. Reid, H.-J. Seo and A. Slosar, *DESI and other dark energy experiments in the era of neutrino mass measurements*, *JCAP* **1405** (2014) 023, [[1308.4164](#)].
- [25] A. Raccanelli, O. Dor, D. J. Bacon, R. Maartens, M. G. Santos et al., *Probing primordial non-Gaussianity via iSW measurements with SKA continuum surveys*, [1406.0010](#).
- [26] S. Camera, M. G. Santos and R. Maartens, *Probing primordial non-Gaussianity with SKA galaxy redshift surveys: a fully relativistic analysis*, [1409.8286](#).
- [27] U. Seljak, *Extracting primordial non-gaussianity without cosmic variance*, *Phys.Rev.Lett.* **102** (2009) 021302, [[0807.1770](#)].
- [28] L. R. Abramo and K. E. Leonard, *Why multi-tracer surveys beat cosmic variance*, *Mon. Not. Roy. Astron. Soc.* **432** (2013) 318, [[1302.5444](#)].
- [29] D. Yamauchi, K. Takahashi and M. Oguri, *Constraining primordial non-Gaussianity via a multitracer technique with surveys by Euclid and Square Kilometre Array*, *Phys.Rev.* **D90** (2014) 083520, [[1407.5453](#)].
- [30] L. D. Ferramacho, M. G. Santos, M. J. Jarvis and S. Camera, *Radio Galaxy populations and the multi-tracer technique: pushing the limits on primordial non-Gaussianity*, *Mon.Not.Roy.Astron.Soc.* **442** (2014) 2511, [[1402.2290](#)].
- [31] D. Alonso and P. G. Ferreira, *Constraining ultralarge-scale cosmology with multiple tracers in optical and radio surveys*, *Phys. Rev.* **D92** (2015) 063525, [[1507.03550](#)].
- [32] J. Fonseca, S. Camera, M. Santos and R. Maartens, *Hunting down horizon-scale effects with multi-wavelength surveys*, *Astrophys. J.* **812** (2015) L22, [[1507.04605](#)].
- [33] R. Scoccimarro, E. Sefusatti and M. Zaldarriaga, *Probing primordial non-Gaussianity with large - scale structure*, *Phys.Rev.* **D69** (2004) 103513, [[astro-ph/0312286](#)].
- [34] E. Sefusatti and E. Komatsu, *The bispectrum of galaxies from high-redshift galaxy surveys: Primordial non-Gaussianity and non-linear galaxy bias*, *Phys.Rev.* **D76** (2007) 083004, [[0705.0343](#)].
- [35] T. Baldauf, U. Seljak and L. Senatore, *Primordial non-Gaussianity in the Bispectrum of the Halo Density Field*, *JCAP* **1104** (2011) 006, [[1011.1513](#)].
- [36] O. Doré et al., *Cosmology with the SPHEREX All-Sky Spectral Survey*, [1412.4872](#).
- [37] D. Jeong and E. Komatsu, *Primordial Non-Gaussianity, Scale-dependent Bias, and the Bispectrum of Galaxies*, *Astrophys. J.* **703** (Oct., 2009) 1230–1248, [[0904.0497](#)].
- [38] G. Tasinato, M. Tellarini, A. J. Ross and D. Wands, *Primordial non-Gaussianity in the bispectra of large-scale structure*, *JCAP* **1403** (2014) 032, [[1310.7482](#)].
- [39] N. Roth and C. Porciani, *Can we really measure f_{NL} from the galaxy power spectrum?*, *Mon. Not. Roy. Astron. Soc.* **425** (Sept., 2012) L81–L85, [[1205.3165](#)].
- [40] L. Dai, E. Pajer and F. Schmidt, *On Separate Universes*, *JCAP* **1510** (2015) 059, [[1504.00351](#)].
- [41] R. de Putter, O. Dor and D. Green, *Is There Scale-Dependent Bias in Single-Field Inflation?*, *JCAP* **1510** (2015) 024, [[1504.05935](#)].
- [42] N. Bartolo, D. Bertacca, M. Bruni, K. Koyama, R. Maartens, S. Matarrese et al., *A relativistic signature in large-scale structure*, [1506.00915](#).
- [43] N. Bartolo, S. Matarrese and A. Riotto, *Signatures of primordial non-Gaussianity in the large-scale*

- structure of the Universe, *JCAP* **0510** (2005) 010, [[astro-ph/0501614](#)].
- [44] T. Tram, C. Fidler, R. Crittenden, K. Koyama, G. W. Pettinari and D. Wands, *The Intrinsic Matter Bispectrum in Λ CDM*, [1602.05933](#).
- [45] E. Di Dio, R. Durrer, G. Marozzi and F. Montanari, *The bispectrum of relativistic galaxy number counts*, *JCAP* **1601** (2016) 016, [[1510.04202](#)].
- [46] D. Huterer, C. E. Cunha and W. Fang, *Calibration errors unleashed: effects on cosmological parameters and requirements for large-scale structure surveys*, *Mon. Not. Roy. Astron. Soc.* **432** (July, 2013) 2945–2961, [[1211.1015](#)].
- [47] A. R. Pullen and C. M. Hirata, *Systematic Effects in Large-Scale Angular Power Spectra of Photometric Quasars and Implications for Constraining Primordial Non-Gaussianity*, *PASP* **125** (June, 2013) 705–718, [[1212.4500](#)].
- [48] N. Agarwal, S. Ho, A. D. Myers, H.-J. Seo, A. J. Ross et al., *Characterizing unknown systematics in large scale structure surveys*, *JCAP* **1404** (2014) 007, [[1309.2954](#)].
- [49] A. J. S. Hamilton, *Linear redshift distortions: A Review*, in *Ringberg Workshop on Large Scale Structure Ringberg, Germany, September 23-28, 1996*, 1997. [astro-ph/9708102](#).
- [50] N. Kaiser, *Clustering in real space and in redshift space*, *Mon. Not. Roy. Astron. Soc.* **227** (1987) 1–27.
- [51] J. C. Jackson, *A critique of Rees’s theory of primordial gravitational radiation*, *Mon. Not. Roy. Astron. Soc.* **156** (1972) 1P.
- [52] H. Gil-Marín, J. Norea, L. Verde, W. J. Percival, C. Wagner et al., *The power spectrum and bispectrum of SDSS DR11 BOSS galaxies I: bias and gravity*, [1407.5668](#).
- [53] K. S. Dawson, D. J. Schlegel, C. P. Ahn, S. F. Anderson, É. Aubourg, S. Bailey et al., *The Baryon Oscillation Spectroscopic Survey of SDSS-III*, *Astron. J.* **145** (Jan., 2013) 10, [[1208.0022](#)].
- [54] K. S. Dawson et al., *The SDSS-IV extended Baryon Oscillation Spectroscopic Survey: Overview and Early Data*, [1508.04473](#).
- [55] DESI collaboration, M. Levi et al., *The DESI Experiment, a whitepaper for Snowmass 2013*, [1308.0847](#).
- [56] R. Laureijs, J. Amiaux, S. Arduini, J. . Auguères, J. Brinchmann, R. Cole et al., *Euclid Definition Study Report, ArXiv e-prints* (Oct., 2011) , [[1110.3193](#)].
- [57] G.-B. Zhao et al., *The extended Baryon Oscillation Spectroscopic Survey (eBOSS): a cosmological forecast*, [1510.08216](#).
- [58] M. Tellarini, A. J. Ross, G. Tasinato and D. Wands, *Non-local bias in the halo bispectrum with primordial non-Gaussianity*, *JCAP* **1507** (2015) 004, [[1504.00324](#)].
- [59] F. Bernardeau, S. Colombi, E. Gaztanaga and R. Scoccimarro, *Large scale structure of the universe and cosmological perturbation theory*, *Phys.Rept.* **367** (2002) 1–248, [[astro-ph/0112551](#)].
- [60] O. Lahav, P. B. Lilje, J. R. Primack and M. J. Rees, *Dynamical effects of the cosmological constant*, *Mon. Not. Roy. Astron. Soc.* **251** (July, 1991) 128–136.
- [61] P. Peebles, *The Large-scale Structure of the Universe*. Princeton series in physics. Princeton University Press, 1980.
- [62] F. R. Bouchet, R. Juszkiewicz, S. Colombi and R. Pellat, *Weakly nonlinear gravitational instability for arbitrary Omega*, *Astrophys. J. Let.* **394** (July, 1992) L5–L8.
- [63] W. H. Press and P. Schechter, *Formation of Galaxies and Clusters of Galaxies by Self-Similar Gravitational Condensation*, *Astrophys. J.* **187** (Feb., 1974) 425–438.
- [64] J. M. Bardeen, J. R. Bond, N. Kaiser and A. S. Szalay, *The statistics of peaks of Gaussian random fields*, *Astrophys. J.* **304** (May, 1986) 15–61.
- [65] J. R. Bond, S. Cole, G. Efstathiou and N. Kaiser, *Excursion set mass functions for hierarchical Gaussian fluctuations*, *Astrophys. J.* **379** (Oct., 1991) 440–460.
- [66] A. R. Zentner, *The Excursion Set Theory of Halo Mass Functions, Halo Clustering, and Halo Growth*, *Int.J.Mod.Phys.* **D16** (2007) 763–816, [[astro-ph/0611454](#)].

- [67] R. K. Sheth and G. Tormen, *Large-scale bias and the peak background split*, *Mon. Not. Roy. Astron. Soc.* **308** (Sept., 1999) 119–126, [[astro-ph/9901122](#)].
- [68] R. K. Sheth, H. J. Mo and G. Tormen, *Ellipsoidal collapse and an improved model for the number and spatial distribution of dark matter haloes*, *Mon. Not. Roy. Astron. Soc.* **323** (May, 2001) 1–12, [[astro-ph/9907024](#)].
- [69] R. K. Sheth and G. Tormen, *An excursion set model of hierarchical clustering: ellipsoidal collapse and the moving barrier*, *Mon. Not. Roy. Astron. Soc.* **329** (Jan., 2002) 61–75, [[astro-ph/0105113](#)].
- [70] M. LoVerde, A. Miller, S. Shandera and L. Verde, *Effects of Scale-Dependent Non-Gaussianity on Cosmological Structures*, *JCAP* **0804** (2008) 014, [[0711.4126](#)].
- [71] M. LoVerde and K. M. Smith, *The non-Gaussian halo mass function with f_{NL} , g_{NL} and τ_{NL}* , *JCAP* **8** (Aug., 2011) 3, [[1102.1439](#)].
- [72] T. Giannantonio and C. Porciani, *Structure formation from non-Gaussian initial conditions: multivariate biasing, statistics, and comparison with N-body simulations*, *Phys.Rev.* **D81** (2010) 063530, [[0911.0017](#)].
- [73] K. M. Smith, S. Ferraro and M. LoVerde, *Halo clustering and g_{NL} -type primordial non-gaussianity*, *JCAP* **1203** (2012) 032, [[1106.0503](#)].
- [74] V. Assassi, D. Baumann and F. Schmidt, *Galaxy Bias and Primordial Non-Gaussianity*, *JCAP* **1512** (2015) 043, [[1510.03723](#)].
- [75] P. Catelan, F. Lucchin, S. Matarrese and C. Porciani, *The bias field of dark matter halos*, *Mon.Not.Roy.Astron.Soc.* **297** (1998) 692–712, [[astro-ph/9708067](#)].
- [76] P. Catelan, C. Porciani and M. Kamionkowski, *Two ways of biasing galaxy formation*, *Mon.Not.Roy.Astron.Soc.* **318** (2000) 39, [[astro-ph/0005544](#)].
- [77] T. Baldauf, U. Seljak, V. Desjacques and P. McDonald, *Evidence for Quadratic Tidal Tensor Bias from the Halo Bispectrum*, *Phys.Rev.* **D86** (2012) 083540, [[1201.4827](#)].
- [78] C.-T. Chiang, C. Wagner, F. Schmidt and E. Komatsu, *Position-dependent power spectrum of the large-scale structure: a novel method to measure the squeezed-limit bispectrum*, *JCAP* **1405** (2014) 048, [[1403.3411](#)].
- [79] T. Matsubara, *The Correlation function in redshift space: General formula with wide angle effects and cosmological distortions*, *Astrophys. J.* **535** (2000) 1, [[astro-ph/9908056](#)].
- [80] A. S. Szalay, T. Matsubara and S. D. Landy, *Redshift space distortions of the correlation function in wide angle galaxy surveys*, *Astrophys. J.* **498** (1998) L1, [[astro-ph/9712007](#)].
- [81] A. F. Heavens and A. N. Taylor, *A Spherical Harmonic Analysis of Redshift Space*, *Mon. Not. Roy. Astron. Soc.* **275** (1995) 483–497, [[astro-ph/9409027](#)].
- [82] M. Tegmark and B. C. Bromley, *Real space cosmic fields from redshift space distributions: A Green function approach*, *Astrophys. J.* **453** (1995) 533, [[astro-ph/9409038](#)].
- [83] S. Zaroubi and Y. Hoffman, *Clustering in Redshift Space: Linear Theory*, *Astrophys. J.* **462** (May, 1996) 25.
- [84] A. J. S. Hamilton and M. Culhane, *Spherical redshift distortions*, *Mon. Not. Roy. Astron. Soc.* **278** (1996) 73, [[astro-ph/9507021](#)].
- [85] I. Szapudi, *Wide angle redshift distortions revisited*, *Astrophys. J.* **614** (2004) 51–55, [[astro-ph/0404477](#)].
- [86] T. Matsubara, *Correlation function in deep redshift space as a cosmological probe*, *Astrophys. J.* **615** (2004) 573–585, [[astro-ph/0408349](#)].
- [87] P. Papai and I. Szapudi, *Non-Perturbative Effects of Geometry in Wide-Angle Redshift Distortions*, *Mon. Not. Roy. Astron. Soc.* **389** (2008) 292, [[0802.2940](#)].
- [88] P. H. F. Reimberg, F. Bernardeau and C. Pitrou, *Redshift-space distortions with wide angular separations*, *JCAP* **1601** (2016) 048, [[1506.06596](#)].
- [89] A. Raccanelli, L. Samushia and W. J. Percival, *Simulating redshift-space distortions for galaxy pairs with wide angular separation*, *Mon. Not. Roy. Astron. Soc.* **409** (Dec., 2010) 1525–1533, [[1006.1652](#)].

- [90] L. Samushia, W. J. Percival and A. Raccanelli, *Interpreting large-scale redshift-space distortion measurements*, *Mon. Not. Roy. Astron. Soc.* **420** (Mar., 2012) 2102–2119, [[1102.1014](#)].
- [91] J. Yoo and U. Seljak, *Wide Angle Effects in Future Galaxy Surveys*, *Mon. Not. Roy. Astron. Soc.* **447** (2015) 1789–1805, [[1308.1093](#)].
- [92] R. Scoccimarro, *Redshift-space distortions, pairwise velocities and nonlinearities*, *Phys. Rev.* **D70** (2004) 083007, [[astro-ph/0407214](#)].
- [93] R. Scoccimarro, H. M. P. Couchman and J. A. Frieman, *The Bispectrum as a signature of gravitational instability in redshift-space*, *Astrophys. J.* **517** (1999) 531–540, [[astro-ph/9808305](#)].
- [94] L. Anderson, É. Aubourg, S. Bailey, F. Beutler, V. Bhardwaj, M. Blanton et al., *The clustering of galaxies in the SDSS-III Baryon Oscillation Spectroscopic Survey: baryon acoustic oscillations in the Data Releases 10 and 11 Galaxy samples*, *MNRAS* **441** (June, 2014) 24–62, [[1312.4877](#)].
- [95] H. Gil-Marín, C. Wagner, J. Norea, L. Verde and W. Percival, *Dark matter and halo bispectrum in redshift space: theory and applications*, *JCAP* **1412** (2014) 029, [[1407.1836](#)].
- [96] H. Gil-Marín, L. Verde, J. Norea, A. J. Cuesta, L. Samushia et al., *The power spectrum and bispectrum of SDSS DR11 BOSS galaxies II: cosmological interpretation*, [1408.0027](#).
- [97] E. Sefusatti, M. Crocce and V. Desjacques, *The halo bispectrum in N-body simulations with non-Gaussian initial conditions*, *Mon. Not. Roy. Astron. Soc.* **425** (Oct., 2012) 2903–2930, [[1111.6966](#)].
- [98] T. Baldauf, M. Mirbabayi, M. Simonovi and M. Zaldarriaga, *LSS constraints with controlled theoretical uncertainties*, [1602.00674](#).
- [99] L. Verde, *A practical guide to Basic Statistical Techniques for Data Analysis in Cosmology*, [0712.3028](#).
- [100] A. Heavens, *Statistical techniques in cosmology*, *ArXiv e-prints* (June, 2009) , [[0906.0664](#)].
- [101] L. Verde, *Statistical Methods in Cosmology*, in *Lecture Notes in Physics, Berlin Springer Verlag* (G. Wolschin, ed.), vol. 800 of *Lecture Notes in Physics, Berlin Springer Verlag*, pp. 147–177, Mar., 2010. [0911.3105](#). DOI.
- [102] R. Scoccimarro, S. Colombi, J. N. Fry, J. A. Frieman, E. Hivon and A. Melott, *Nonlinear evolution of the bispectrum of cosmological perturbations*, *Astrophys. J.* **496** (1998) 586, [[astro-ph/9704075](#)].
- [103] M. Liguori, E. Sefusatti, J. R. Fergusson and E. P. S. Shellard, *Primordial Non-Gaussianity and Bispectrum Measurements in the Cosmic Microwave Background and Large-Scale Structure*, *Advances in Astronomy* **2010** (2010) 980523, [[1001.4707](#)].
- [104] E. Sefusatti, M. Crocce, S. Pueblas and R. Scoccimarro, *Cosmology and the Bispectrum*, *Phys. Rev.* **D74** (2006) 023522, [[astro-ph/0604505](#)].
- [105] PLANCK collaboration, P. A. R. Ade et al., *Planck 2015 results. XIII. Cosmological parameters*, [1502.01589](#).
- [106] L. Verde, A. F. Heavens, W. J. Percival, S. Matarrese, C. M. Baugh et al., *The 2dF Galaxy Redshift Survey: The Bias of galaxies and the density of the Universe*, *Mon. Not. Roy. Astron. Soc.* **335** (2002) 432, [[astro-ph/0112161](#)].
- [107] Y. Jing and G. Boerner, *The three-point correlation function of galaxies determined from the 2df galaxy redshift survey*, *Astrophys. J.* **607** (2004) 140–163, [[astro-ph/0311585](#)].
- [108] E. Gaztanaga, P. Norberg, C. Baugh and D. Croton, *Statistical analysis of galaxy surveys. 2. The 3-point galaxy correlation function measured from the 2dFGRS*, *Mon. Not. Roy. Astron. Soc.* **364** (2005) 620–634, [[astro-ph/0506249](#)].
- [109] F. Marín, *The Large-scale Three-point Correlation Function of Sloan Digital Sky Survey Luminous Red Galaxies*, *Astrophys. J.* **737** (Aug., 2011) 97, [[1011.4530](#)].
- [110] C. K. McBride, A. J. Connolly, J. P. Gardner, R. Scranton, R. Scoccimarro, A. A. Berlind et al., *Three-point Correlation Functions of SDSS Galaxies: Constraining Galaxy-mass Bias*, *Astrophys. J.* **739** (Oct., 2011) 85, [[1012.3462](#)].
- [111] WIGGLEZ collaboration, F. A. Marin et al., *The WiggleZ Dark Energy Survey: constraining galaxy bias and cosmic growth with 3-point correlation functions*, *Mon. Not. Roy. Astron. Soc.* **432** (2013) 2654, [[1303.6644](#)].

- [112] C.-T. Chiang, C. Wagner, A. G. Sanchez, F. Schmidt and E. Komatsu, *Position-dependent correlation function from the SDSS-III Baryon Oscillation Spectroscopic Survey Data Release 10 CMASS Sample*, *JCAP* **1509** (2015) 028, [[1504.03322](#)].

A Halo mass function and Lagrangian bias

Through this paper we assume a mass function,

$$n_g(M, z) = f(\nu) \frac{\rho_m}{M} \left| \frac{d \ln \sigma}{dM} \right|, \quad (\text{A.1})$$

with $f = f_{\text{ST}} (f_{\text{LV}}/f_{\text{PS}})$. The Press-Schechter mass function f_{PS} [63] for Gaussian initial conditions and spherical collapse is

$$f_{\text{PS}}(\nu) = \sqrt{\frac{2}{\pi}} \nu e^{-\frac{\nu^2}{2}}, \quad (\text{A.2})$$

while, allowing for ellipsoidal collapse, the Sheth-Tormen mass function f_{ST} [67–69] is obtained:

$$f_{\text{ST}}(\nu) = A(p) \sqrt{\frac{2\gamma}{\pi}} \left[1 + (\gamma\nu^2)^{-p} \right] \nu e^{-\gamma \frac{\nu^2}{2}}. \quad (\text{A.3})$$

By fitting against simulations, one finds the parameters $\gamma = 0.707$ and $p = 0.3$. Then, requiring all the mass to be collapsed into halos gives $A(p) = 0.322$.

By approximating a weakly non-Gaussian initial state with an Edgeworth expansion, the Lo Verde *et al* mass function f_{LV} [70] is found

$$f_{\text{LV}}(\nu, M) = f_{\text{PS}}(\nu) \left[1 + \frac{1}{6} \left(\kappa_3(M) H_3(\nu) - \frac{d\kappa_3(M)/dM}{d \ln \sigma^{-1}/dM} \frac{H_2(\nu)}{\nu} \right) \right], \quad (\text{A.4})$$

where the function H_n is the n -th Hermite polynomial and the 3rd cumulant $\kappa_3(M)$ is defined as $\kappa_3(M) = \langle \delta_{\text{lin}}^3 \rangle / \sigma^3$ with

$$\begin{aligned} \langle \delta_{\text{lin}}^3 \rangle = \int \frac{d^3 p}{(2\pi)^3} \int \frac{d^3 p'}{(2\pi)^3} \int \frac{d^3 p''}{(2\pi)^3} W_M(p) \alpha(p, z) W_M(p') \alpha(p', z) W_M(p'') \alpha(p'', z) \times \\ \times \langle \Phi_{\text{in}}(\mathbf{p}) \Phi_{\text{in}}(\mathbf{p}') \Phi_{\text{in}}(\mathbf{p}'') \rangle. \end{aligned} \quad (\text{A.5})$$

A convenient fitting function for $\kappa_3(M)$ is given in eq. (2.17). Also, for primordial non-Gaussianity of the form of eq. (1.1), the variance gets a correction proportional to f_{NL}^2 , that can be written as

$$\begin{aligned} \sigma^2 = \langle \delta_{\text{lin}}^2 \rangle = \int \frac{d^3 p}{(2\pi)^3} \int \frac{d^3 p'}{(2\pi)^3} W_M(p) \alpha(p, z) W_M(p') \alpha(p', z) \langle \Phi_{\text{in}}(\mathbf{p}) \Phi_{\text{in}}(\mathbf{p}') \rangle \\ \approx \sigma_G^2 (1 + \kappa_2(M)). \end{aligned} \quad (\text{A.6})$$

Since κ_2 gives a negligible correction to the Gaussian variance $\sigma_G = \langle \delta_G^2 \rangle$ for any realistic value of f_{NL} [71], we neglect it. Although the LV mass function is no longer universal, as it formally depends not only on ν but also on the mass M , the extra dependence on M through eqs. (2.17) and (A.6) is weak and we practically treat f_{LV} as universal.

As explained in section 2.3, local type PNG introduces in the mass function an additional dependence on the local effective variance σ_l , so that the halo/galaxy overdensity acquires a bivariate form

$$\begin{aligned} \delta_g^L(\mathbf{q}) = \beta_{10} \delta_{\text{lin},l} + \beta_{01} \left(\frac{\sigma_l}{\sigma} - 1 \right) + \\ + \frac{1}{2} \left[\beta_{20} (\delta_{\text{lin},l})^2 + \beta_{02} \left(\frac{\sigma_l}{\sigma} - 1 \right)^2 + 2\beta_{11} \delta_{\text{lin},l} \left(\frac{\sigma_l}{\sigma} - 1 \right) \right], \end{aligned} \quad (\text{A.7})$$

with the bias coefficients defined as

$$\beta_{ij} \equiv \left[\frac{(\sigma_l)^j}{n_h} \frac{\partial^{i+j} n_g}{(\partial \delta_{\text{lin},l})^i (\partial \sigma_l)^j} \right] \Big|_{\delta_{\text{lin},l}=0, \sigma_l=\sigma}. \quad (\text{A.8})$$

By using the explicit form of eq. (2.21) for σ_l and redefining the bias as

$$\begin{aligned} b_{10}^L &= \beta_{10}, \\ b_{01}^L &= 2f_{\text{NL}}\beta_{01}, \\ b_{20}^L &= \frac{\beta_{20}}{2}, \\ b_{11}^L &= 2f_{\text{NL}}\beta_{11}, \\ b_{02}^L &= 2f_{\text{NL}}^2\beta_{02}, \end{aligned} \quad (\text{A.9})$$

that we call *Lagrangian bias coefficients*, one can then easily obtain the bivariate model in the form quoted in eq. (2.22). By using the mass function of eq. (2.16) in the definition of eq. (A.8), the linear and non-linear Lagrangian bias coefficients read

$$b_{10}^L = \frac{\gamma\nu^2 - 1}{\delta_c} + \frac{2p}{1 + (\gamma\nu^2)^p} \frac{1}{\delta_c} - \kappa_3 \frac{\nu^3 - \nu}{2\delta_c} + \frac{d\kappa_3/dM}{d \ln \sigma^{-1}/dM} \frac{\nu + \nu^{-1}}{6\delta_c} \quad (\text{A.10})$$

$$\begin{aligned} b_{20}^L &= \gamma\nu^2 \frac{\gamma\nu^2 - 3}{2\delta_c^2} + \frac{p}{1 + (\gamma\nu^2)^p} \frac{2\gamma\nu^2 + 2p - 1}{\delta_c^2} - \frac{\kappa_3}{2} \left[\frac{\gamma\nu^5 - (\gamma + 2)\nu^3 + \nu}{\delta_c^2} + \frac{2p}{1 + (\gamma\nu^2)^p} \frac{\nu^3 - \nu}{\delta_c^2} \right] + \\ &+ \frac{1}{2} \frac{d\kappa_3/dM}{d \ln \sigma^{-1}/dM} \left[\frac{\gamma\nu^3 + (\gamma - 1)\nu}{3\delta_c^2} + \frac{2p}{1 + (\gamma\nu^2)^p} \frac{\nu - \nu^{-1}}{3\delta_c^2} \right], \end{aligned} \quad (\text{A.11})$$

while all the non-Gaussian bias factors are built from a combination of these:

$$\begin{aligned} b_{01}^L &= 2f_{\text{NL}}\delta_c b_{10}^L, \\ b_{11}^L &= 2f_{\text{NL}}(\delta_c b_{20}^L - b_{10}^L), \\ b_{02}^L &= 4f_{\text{NL}}^2\delta_c(\delta_c b_{20}^L - 2b_{10}^L). \end{aligned} \quad (\text{A.12})$$

B Position-dependent power spectrum

Although the bispectrum contains more information than power spectrum, it is more challenging to measure and, indeed, only few measurements have been reported so far [33, 52, 96, 106–111]. To overcome this issue, a new observable has been proposed in [78], which measures an integral of the squeezed configuration of the bispectrum. In [112], this has been applied to measure the non-linear bias b_{20} from the BOSS data release 10.

This new observable, called *position-dependent power spectrum*, correlates the power spectrum in a subvolume of the survey volume to the mean overdensity of the subvolume itself: basically it measure the response of the spectra of short density modes to a large-scale fluctuation. We briefly describe below how the position-dependent power spectrum is built, referring the reader to [78, 112] for further details.

Given a density field $\delta(\mathbf{x})$ in a cubic survey volume V with length side L_B , suppose to split it into N subvolumes, with side $L = L_B/N$. If we now focus on the subvolume centred at \mathbf{x}_L , we can measure the local mean overdensity as

$$\bar{\delta}(\mathbf{x}_L) = \frac{1}{V_L} \int d^3x \delta(\mathbf{x}) W_L(\mathbf{x} - \mathbf{x}_L), \quad (\text{B.1})$$

where the volume of the subvolume is $V_L = L^3$ and the window function is assumed to be

$$W_L(\mathbf{x}) = \prod_{i=1}^3 \theta(x_i), \quad \theta(x_i) = \begin{cases} 1, & |x_i| \leq L/2, \\ 0, & \text{otherwise.} \end{cases} \quad (\text{B.2})$$

The Fourier transform of the window is $W_L(\mathbf{k}) = L^3 \prod_{i=1}^3 j_0(k_i L/2)$, where the 0-th spherical Bessel function is $j_0(x) = \sin(x)/x$. The position-dependent power spectrum is defined as

$$P(\mathbf{k}, \mathbf{x}_L) \equiv \frac{1}{V_L} |\delta(\mathbf{k}, \mathbf{x}_L)|^2, \quad (\text{B.3})$$

where $\delta(\mathbf{k}, \mathbf{x}_L) \equiv \int_{V_L} d^3x \delta(\mathbf{x}) e^{-i\mathbf{x}\cdot\mathbf{k}}$ is the Fourier transformation of the density field with integral ranging over the subvolume centred at \mathbf{x}_L .

If we now correlate the mean overdensity to the position-dependent power spectrum in the corresponding subvolume, it can be shown that

$$\langle P(\mathbf{k}, \mathbf{x}_L) \bar{\delta}(\mathbf{x}_L) \rangle = \frac{1}{V_L^2} \int \frac{d^3p_1}{(2\pi)^3} \int \frac{d^3p_3}{(2\pi)^3} B(\mathbf{k} - \mathbf{p}_1, -\mathbf{k} + \mathbf{p}_1 + \mathbf{p}_3, -\mathbf{p}_3) \times \quad (\text{B.4})$$

$$\times W_L(\mathbf{p}_1) W_L(-\mathbf{p}_1 - \mathbf{p}_3) W_L(\mathbf{p}_3) \equiv iB(\mathbf{k}), \quad (\text{B.5})$$

where $iB(\mathbf{k})$ is called the *integrated bispectrum* and $B(\mathbf{k}_1, \mathbf{k}_2, \mathbf{k}_3)$ can be the matter bispectrum, the galaxy bispectrum or cross-correlations between matter and galaxies. An angular average over $iB(\mathbf{k})$ removes the remaining \mathbf{k} -dependence due to the choice of a cubic window function and one finally gets

$$iB(k) \equiv \int \frac{d^2\Omega_{\mathbf{k}}}{4\pi} iB(\mathbf{k}) = \frac{1}{V_L^2} \int \frac{d^2\Omega_{\mathbf{k}}}{4\pi} \int \frac{d^3p_1}{(2\pi)^3} \int \frac{d^3p_3}{(2\pi)^3} B(\mathbf{k} - \mathbf{p}_1, -\mathbf{k} + \mathbf{p}_1 + \mathbf{p}_3, -\mathbf{p}_3) \times \quad (\text{B.6})$$

$$\times W_L(\mathbf{p}_1) W_L(-\mathbf{p}_1 - \mathbf{p}_3) W_L(\mathbf{p}_3).$$

From the behaviour of the 0-th spherical Bessel function, the dominant contribution to the integrated bispectrum comes from wavenumbers \mathbf{k} that are larger than $1/L$, i.e. from the squeezed configuration of the bispectrum $B(\mathbf{k} - \mathbf{p}_1, -\mathbf{k} + \mathbf{p}_1 + \mathbf{p}_3, -\mathbf{p}_3) \rightarrow B(\mathbf{k}, -\mathbf{k}, -\mathbf{p}_3)$ with $p_1 \ll k$ and $p_3 \ll k$.

If we consider the tree-level matter bispectrum with Gaussian initial conditions ($f_{\text{NL}} = 0$),

$$B_{mmm}^G(\mathbf{k}_1, \mathbf{k}_2, \mathbf{k}_3) = 2[P(k_1)P(k_2)F_2(\mathbf{k}_1, \mathbf{k}_2) + 2 \text{ perm}], \quad (\text{B.7})$$

it can be shown that the integrated bispectrum is [78]

$$iB_{mmm}^G(k) \stackrel{kL \rightarrow \infty}{\equiv} \left[\frac{68}{21} - \frac{1}{3} \frac{d \ln k^3 P(k)}{d \ln k} \right] P(k) \sigma_L^2, \quad (\text{B.8})$$

where σ_L^2 is the variance of the density field on the subvolume scale,

$$\sigma_L^2 \equiv \frac{1}{V_L^2} \int \frac{d^3p_3}{(2\pi)^3} W_L^2(\mathbf{p}_3) P(p_3). \quad (\text{B.9})$$

By including local type PNG, the tree-level matter bispectrum reads

$$B_{mmm}(\mathbf{k}_1, \mathbf{k}_2, \mathbf{k}_3) = 2 \left[\mathcal{F}_2(\mathbf{k}_1, \mathbf{k}_2) + f_{\text{NL}} \frac{\alpha(k_3)}{\alpha(k_1)\alpha(k_2)} \right] P(k_1)P(k_2) + 2 \text{ cyc.} \quad (\text{B.10})$$

and the linear response of the small-scale matter power spectrum to large-scale density perturbation is now

$$iB_{mmm}(k) \stackrel{kL \rightarrow \infty}{\equiv} \left[\frac{68}{21} - \frac{1}{3} \frac{d \ln k^3 P(k)}{d \ln k} \right] P(k) \sigma_L^2 + 4f_{\text{NL}} \sigma_{\text{nG},1}^2 P(k) + 2f_{\text{NL}} \sigma_{\alpha}^2 \frac{P^2(k)}{\alpha^2(k)}, \quad (\text{B.11})$$

where we have introduced the new quantities

$$\sigma_{\text{nG},i}^2 \equiv \frac{1}{V_L^2} \int \frac{d^3p_3}{(2\pi)^3} W_L^2(\mathbf{p}_3) \frac{P(p_3)}{\alpha^i(p_3)}, \quad (\text{B.12})$$

$$\sigma_\alpha^2 \equiv \frac{1}{V_L^2} \int \frac{d^3 p_3}{(2\pi)^3} W_L^2(\mathbf{p}_3) \alpha(p_3). \quad (\text{B.13})$$

If we now consider the galaxy bispectrum of eq. (2.32), the integrated bispectrum is

$$\begin{aligned} iB_{ggg}(k) \stackrel{kL \rightarrow \infty}{=} P(k) \sigma_L^2 & \left\{ \left[b_{10}^3 \left(\frac{68}{21} - \frac{1}{3} \frac{d \ln k^3 P(k)}{d \ln k} \right) + 4b_{10}^2 b_{20} \right] + \right. \\ & \left. + \frac{1}{\alpha(k)} \left[b_{10}^2 b_{11} + 2b_{10} b_{01} b_{20} + b_{10}^2 b_{01} \left(\frac{68}{21} - \frac{1}{3} \frac{d \ln k^3 P(k)}{d \ln k} \right) \right] + 2 \frac{b_{10} b_{01} b_{11}}{\alpha^2(k)} \right\} + \\ & + P(k) \sigma_{\text{NG},1}^2 \left\{ \left[b_{10}^2 b_{01} \left(\frac{68}{21} - \frac{1}{3} \frac{d \ln k^3 P(k)}{d \ln k} \right) + 2b_{10}^2 b_{11} + 2b_{10} b_{01} b_{20} + 4f_{\text{NL}} b_{10}^3 \right] + \right. \\ & \left. + \frac{1}{\alpha(k)} \left[b_{10}^2 b_{01} \left(\frac{68}{21} - \frac{1}{3} \frac{d \ln k^3 P(k)}{d \ln k} \right) + 4b_{10}^2 b_{02} + 2b_{10} b_{01} b_{11} + 4b_{01}^2 b_{20} \right] + \right. \\ & \left. + \frac{2}{\alpha(k)^2} \left[b_{01}^2 b_{11} + 2b_{10} b_{01} b_{02} \right] \right\} + \\ & + P(k) \sigma_{\text{NG},2}^2 \left\{ 2 \left(b_{10} b_{01} b_{11} + 2f_{\text{NL}} b_{10}^2 b_{01} \right) + \right. \\ & \left. + \frac{2}{\alpha(k)} \left(b_{01}^2 b_{11} + 2b_{10} b_{01} b_{02} + 2f_{\text{NL}} b_{10} b_{01}^2 \right) + 4 \frac{b_{01}^2 b_{02}}{\alpha^2(k)} \right\} + \\ & + P^2(k) \sigma_\alpha^2 \left\{ \frac{2f_{\text{NL}}}{\alpha(k)} \left[b_{10}^3 + \frac{1}{\alpha^3(k)} \left(b_{10}^2 b_{01} + b_{10} b_{01}^2 \right) \right] \right\} + \\ & + \frac{P^2(k)}{V_L} \left\{ 2 \left(b_{10}^2 b_{20} - \frac{4}{21} b_{10}^2 b_{10}^L \right) + \frac{2}{\alpha(k)} \left(b_{10}^2 b_{11} + b_{10} b_{01} b_{20} - \frac{8}{21} b_{10} b_{01} b_{10}^L + b_{10}^2 b_{01} \right) + \right. \\ & \left. + \frac{2}{\alpha^2(k)} \left(b_{10}^2 b_{02} + 2b_{10} b_{01} b_{11} + b_{01}^2 b_{20} - \frac{4}{21} b_{01}^2 b_{10}^L + 2b_{10} b_{01}^2 + 2b_{01}^3 \right) + \right. \\ & \left. + \frac{2}{\alpha^4(k)} \left(b_{01}^2 b_{02} + 2b_{10} b_{01} b_{02} \right) \right\}. \quad (\text{B.14}) \end{aligned}$$

Equations (B.11) and (B.14) are our prediction for $iB(k)$ coming from the matter and galaxy bispectrum with local-type non-Gaussianity, respectively. In [112], an analysis on iB_{ggg} shows poor constraints on f_{NL} compared to those from the power spectrum. However, since the scale-dependent bias due to local-type non-Gaussianity was ignored there, it would be interesting to see how much the constraint on f_{NL} from the position-dependent power spectrum would improve when the result of eq. (B.14) is used. We leave this for future work.

C \mathcal{D} factors

The factors $\mathcal{D}(k_i, k_j, \cos \theta_{ij}, y_{ij}, \beta)$ introduced in section 3.2 are defined as the integrals below

$$\mathcal{D}_{\text{SQ1}} = \frac{1}{4\pi} \int_{-1}^{+1} d\mu_1 \int_0^{2\pi} d\phi 2(1 + \beta\mu_i^2)(1 + \beta\mu_j^2) \quad (\text{C.1})$$

$$\mathcal{D}_{\text{NLB}} = \mathcal{D}_{\text{SQ1}} \quad (\text{C.2})$$

$$\mathcal{D}_{\text{SQ2}} = \frac{1}{4\pi} \int_{-1}^{+1} d\mu_1 \int_0^{2\pi} d\phi 2\beta\mu_k^2 (1 + \beta\mu_i^2)(1 + \beta\mu_j^2) \quad (\text{C.3})$$

$$\mathcal{D}_{\text{FOG}} = \frac{1}{4\pi} \int_{-1}^{+1} d\mu_1 \int_0^{2\pi} d\phi \beta\mu_k k_k (1 + \beta\mu_i^2)(1 + \beta\mu_j^2) \left[\beta\mu_k k_k \frac{\mu_i}{k_i} \frac{\mu_j}{k_j} - \left(\frac{\mu_i}{k_i} + \frac{\mu_j}{k_j} \right) \right] \quad (\text{C.4})$$

$$\mathcal{D}_{\text{nG2}} = \mathcal{D}_{\text{SQ1}} \quad (\text{C.5})$$

$$\mathcal{D}_{\text{FoGnG}} = -\frac{1}{4\pi} \int_{-1}^{+1} d\mu_1 \int_0^{2\pi} d\phi \beta \mu_k k_k (1 + \beta \mu_i^2) (1 + \beta \mu_j^2) \left(\frac{\mu_i}{k_i \alpha(k_j)} + \frac{\mu_j}{k_j \alpha(k_i)} \right) \quad (\text{C.6})$$

$$\mathcal{D}_{\text{SQ1}}^{\text{nG1}} = \frac{1}{4\pi} \int_{-1}^{+1} d\mu_1 \int_0^{2\pi} d\phi 2 \left(\frac{1 + \beta \mu_i^2}{\alpha(k_j)} + \frac{1 + \beta \mu_j^2}{\alpha(k_i)} \right) \quad (\text{C.7})$$

$$\mathcal{D}_{\text{NLB}}^{\text{nG1}} = \mathcal{D}_{\text{SQ1}}^{\text{nG1}} \quad (\text{C.8})$$

$$\mathcal{D}_{\text{SQ2}}^{\text{nG1}} = \frac{1}{4\pi} \int_{-1}^{+1} d\mu_1 \int_0^{2\pi} d\phi 2\beta \mu_k^2 \left(\frac{1 + \beta \mu_i^2}{\alpha(k_j)} + \frac{1 + \beta \mu_j^2}{\alpha(k_i)} \right) \quad (\text{C.9})$$

$$\mathcal{D}_{\text{FOG}}^{\text{nG1}} = \frac{1}{4\pi} \int_{-1}^{+1} d\mu_1 \int_0^{2\pi} d\phi \beta \mu_k k_k \left(\frac{1 + \beta \mu_i^2}{\alpha(k_j)} + \frac{1 + \beta \mu_j^2}{\alpha(k_i)} \right) \left[\beta \mu_k k_k \frac{\mu_i}{k_i} \frac{\mu_j}{k_j} - \left(\frac{\mu_i}{k_i} + \frac{\mu_j}{k_j} \right) \right] \quad (\text{C.10})$$

$$\mathcal{D}_{\text{nG2}}^{\text{nG1}} = \mathcal{D}_{\text{SQ1}}^{\text{nG1}} \quad (\text{C.11})$$

$$\mathcal{D}_{\text{FoGnG}}^{\text{nG1}} = -\frac{1}{4\pi} \int_{-1}^{+1} d\mu_1 \int_0^{2\pi} d\phi \beta \mu_k k_k \left(\frac{1 + \beta \mu_i^2}{\alpha(k_j)} + \frac{1 + \beta \mu_j^2}{\alpha(k_i)} \right) \left(\frac{\mu_i}{k_i \alpha(k_j)} + \frac{\mu_j}{k_j \alpha(k_i)} \right) \quad (\text{C.12})$$

$$\mathcal{D}_{\text{SQ2}}^{\text{nG1}^2} = \frac{1}{4\pi} \int_{-1}^{+1} d\mu_1 \int_0^{2\pi} d\phi \frac{2\beta \mu_k^2}{\alpha(k_i) \alpha(k_j)} \quad (\text{C.13})$$

$$\mathcal{D}_{\text{FOG}}^{\text{nG1}^2} = \frac{1}{4\pi} \int_{-1}^{+1} d\mu_1 \int_0^{2\pi} d\phi \beta \frac{\mu_k k_k}{\alpha(k_i) \alpha(k_j)} \left[\beta \mu_k k_k \frac{\mu_i}{k_i} \frac{\mu_j}{k_j} - \left(\frac{\mu_i}{k_i} + \frac{\mu_j}{k_j} \right) \right] \quad (\text{C.14})$$

$$\mathcal{D}_{\text{FoGnG}}^{\text{nG1}^2} = -\frac{1}{4\pi} \int_{-1}^{+1} d\mu_1 \int_0^{2\pi} d\phi \beta \frac{\mu_k k_k}{\alpha(k_i) \alpha(k_j)} \left(\frac{\mu_i}{k_i \alpha(k_j)} + \frac{\mu_j}{k_j \alpha(k_i)} \right), \quad (\text{C.15})$$

yielding the following results

$$\mathcal{D}_{\text{SQ1}} = \frac{2}{15} [15 + 10\beta + \beta^2 (2x_{ij}^2 + 1)] \quad (\text{C.16})$$

$$\mathcal{D}_{\text{NLB}} = \mathcal{D}_{\text{SQ1}} \quad (\text{C.17})$$

$$\mathcal{D}_{\text{SQ2}} = \frac{2\beta}{105 (2x_{ij} y_{ij} + y_{ij}^2 + 1)} \left[12\beta^2 y_{ij} x_{ij}^3 + 2\beta x_{ij}^2 (6\beta + 7) (y_{ij}^2 + 1) + 2x_{ij} y_{ij} (9\beta^2 + 42\beta + 35) + (3\beta^2 + 28\beta + 35) (y_{ij}^2 + 1) \right] \quad (\text{C.18})$$

$$\mathcal{D}_{\text{FOG}} = \frac{\beta}{315 y_{ij}} \left[16\beta^3 y_{ij} x_{ij}^4 + 4\beta^2 x_{ij}^3 (5\beta + 9) (y_{ij}^2 + 1) + 24\beta x_{ij}^2 y_{ij} (2\beta^2 + 9\beta + 7) + 3x_{ij} (5\beta^3 + 33\beta^2 + 63\beta + 35) (y_{ij}^2 + 1) + 6y_{ij} (\beta^3 + 9\beta^2 + 35\beta + 35) \right] \quad (\text{C.19})$$

$$\mathcal{D}_{\text{nG2}} = \mathcal{D}_{\text{SQ1}} \quad (\text{C.20})$$

$$\mathcal{D}_{\text{FoGnG}} = \frac{\beta}{105 \alpha(k_i) \alpha(k_j) y_{ij}} \left[6\beta^2 x_{ij}^3 (\alpha(k_1) + \alpha(k_2) y_{ij}^2) + 2\beta (6\beta + 7) x_{ij}^2 y_{ij} (\alpha(k_i) + \alpha(k_j)) + (9\beta^2 + 42\beta + 35) x_{ij} (\alpha(k_i) + \alpha(k_j) y_{ij}^2) + (3\beta^2 + 28\beta + 35) y_{ij} (\alpha(k_i) + \alpha(k_j)) \right] \quad (\text{C.21})$$

$$\mathcal{D}_{\text{SQ1}}^{\text{nG1}} = \frac{2}{3} (3 + \beta) \left(\frac{1}{\alpha(k_i)} + \frac{1}{\alpha(k_j)} \right) \quad (\text{C.22})$$

$$\mathcal{D}_{\text{NLB}}^{\text{nG1}} = \mathcal{D}_{\text{SQ1}}^{\text{nG1}} \quad (\text{C.23})$$

$$\mathcal{D}_{\text{SQ2}}^{\text{nG1}} = \frac{2\beta}{15 \alpha(k_i) \alpha(k_j) (2x_{ij} y_{ij} + y_{ij}^2 + 1)} \left[\alpha(k_i) (\beta + 2\beta x_{ij}^2 + 2(3\beta + 5) x_{ij} y_{ij} + (3\beta + 5) y_{ij}^2 + 5) + \alpha(k_j) (3\beta + 2\beta x_{ij}^2 y_{ij}^2 + 2(3\beta + 5) x_{ij} y_{ij} + (\beta + 5) y_{ij}^2 + 5) \right] \quad (\text{C.24})$$

$$\mathcal{D}_{\text{FOG}}^{\text{nG1}} = \frac{\beta}{105\alpha(k_i)\alpha(k_j)y_{ij}} \left[6\beta^2 x_{ij}^3 (\alpha(k_i) + \alpha(k_j)y_{ij}^2) + 6\beta(4\beta + 7)x_{ij}^2 y_{ij} (\alpha(k_i) + \alpha(k_j)) + \right. \\ \left. + x_{ij} \left((\alpha(k_i) (9\beta^2 + 42\beta + (15\beta^2 + 42\beta + 35) y_{ij}^2) + 35) + \right. \right. \\ \left. \left. + \alpha(k_j) (15\beta^2 + 42\beta + (9\beta^2 + 42\beta + 35) y_{ij}^2 + 35) \right) + \right. \\ \left. 2(3\beta^2 + 21\beta + 35) y_{ij} (\alpha(k_i) + \alpha(k_j)) \right] \quad (\text{C.25})$$

$$\mathcal{D}_{\text{nG2}}^{\text{nG1}} = \mathcal{D}_{\text{SQ1}}^{\text{nG1}} \quad (\text{C.26})$$

$$\mathcal{D}_{\text{FoGnG}}^{\text{nG1}} = \frac{\beta}{15\alpha(k_i)^2\alpha(k_j)^2y_{ij}} \left[4\alpha(k_i)\alpha(k_j)\beta x_{ij}^2 y_{ij} + \right. \\ \left. + (3\beta + 5)x_{ij} (\alpha(k_i)^2 + \alpha(k_i)\alpha(k_j) (y_{ij}^2 + 1) + \alpha(k_j)^2 y_{ij}^2) + \right. \\ \left. + y_{ij} (\alpha(k_i)^2(3\beta + 5) + 2\alpha(k_i)\alpha(k_j)(\beta + 5) + \alpha(k_j)^2(3\beta + 5)) \right] \quad (\text{C.27})$$

$$\mathcal{D}_{\text{SQ2}}^{\text{nG1}^2} = \frac{2}{3} \frac{\beta}{\alpha(k_i)\alpha(k_j)} \quad (\text{C.28})$$

$$\mathcal{D}_{\text{FOG}}^{\text{nG1}^2} = \frac{\beta}{15\alpha(k_i)\alpha(k_j)y_{ij}} \left[4\beta x_{ij}^2 y_{ij} + (3\beta + 5)x_{ij} (y_{ij}^2 + 1) + 2(\beta + 5)y_{ij} \right] \quad (\text{C.29})$$

$$\mathcal{D}_{\text{FoGnG}}^{\text{nG1}^2} = \frac{\beta}{3\alpha(k_i)^2\alpha(k_j)^2y_{ij}} \left[x_{ij} (\alpha(k_i) + \alpha(k_j)y_{ij}^2) + y_{ij} (\alpha(k_i) + \alpha(k_j)) \right], \quad (\text{C.30})$$

where $x_{ij} = (\mathbf{k}_i \cdot \mathbf{k}_j)/k_i k_j$ and $y_{ij} = k_i/k_j$.

D Basic numbers for BOSS, eBOSS, DESI, Euclid

Here we present tables with the numbers describing the BOSS, DESI, Euclid [24] and eBOSS [57] surveys, which we use to forecast constraints on primordial non-Gaussianity in section 4.

Table 2: Basic numbers for BOSS LRGs. The shell volume V is in units of $(\text{Gpc}/h)^3$, while the number density N_{LRG} in $10^{-4} (h/\text{Mpc})^3$. The fiducial value for b_{10}^{LRG} and the estimates of ν_{LRG} and the non-linear bias b_{20}^{LRG} are also presented.

z	V	N_{LRG}	b_{10}^{LRG}	ν_{LRG}	b_{20}^{LRG}
0.05	0.03	3.14	1.74	1.68	-0.04
0.15	0.16	3.06	1.84	1.74	0.02
0.25	0.40	3.12	1.94	1.81	0.09
0.35	0.70	3.17	2.04	1.88	0.18
0.45	1.03	3.21	2.15	1.95	0.29
0.55	1.38	3.25	2.26	2.01	0.41
0.65	1.71	1.22	2.37	2.08	0.55
0.75	2.03	0.15	2.49	2.15	0.70

Table 3: Basic numbers for eBOSS LRGs. The shell volume V is in units of $(\text{Gpc}/h)^3$, while the number density N_{LRG} in $10^{-4} (h/\text{Mpc})^3$. The fiducial value for b_{10}^{LRG} and the estimates of ν_{LRG} and the non-linear bias b_{20}^{LRG} are also presented.

z	V	N_{LRG}	b_{10}^{LRG}	ν_{LRG}	b_{20}^{LRG}
0.65	1.20	0.810	2.37	2.08	0.55
0.75	1.42	0.678	2.49	2.15	0.70
0.85	1.63	0.350	2.61	2.21	0.87
0.95	1.82	0.097	2.73	2.28	1.06

Table 4: Basic numbers for eBOSS QSOs. The shell volume V is in units of $(\text{Gpc}/h)^3$, while the number density N_{QSO} in $10^{-4} (h/\text{Mpc})^3$. The fiducial value for b_{10}^{QSO} and the estimates of ν_{QSO} and the non-linear bias b_{20}^{QSO} are also presented.

z	V	N_{QSO}	b_{10}^{QSO}	ν_{QSO}	b_{20}^{QSO}
0.65	1.28	0.119	1.32	1.33	-0.22
0.75	1.52	0.130	1.42	1.42	-0.19
0.85	1.74	0.154	1.52	1.51	-0.16
0.95	1.95	0.171	1.63	1.59	-0.11
1.05	2.12	0.163	1.75	1.68	-0.04
1.15	2.28	0.170	1.87	1.77	0.04
1.30	4.96	0.175	2.06	1.89	0.21
1.50	5.36	0.166	2.34	2.06	0.51
1.70	5.65	0.151	2.64	2.23	0.93
1.90	5.84	0.137	2.97	2.40	1.48
2.05	2.96	0.122	3.23	2.53	1.99
2.15	2.98	0.093	3.41	2.61	2.39

Table 5: Basic numbers for eBOSS ELGs. The labels Fisher, LD, HD stand respectively for Fisher Discriminant, Low Density DECam and High Density DECam selected objects. The shell volume V is in units of $(\text{Gpc}/h)^3$, while the expected number density N_X based on target selection definition X is in $10^{-4} (h/\text{Mpc})^3$. The fiducial value for b_{10}^{ELG} and the estimates of ν_{ELG} and the non-linear bias b_{20}^{ELG} are also presented.

z	V	N_{Fisher}	N_{LD}	N_{HD}	b_{10}^{ELG}	ν_{ELG}	b_{20}^{ELG}
0.65	0.26	1.41	0.183	0.205	1.40	1.40	-0.20
0.75	0.30	2.17	1.91	2.07	1.46	1.46	-0.18
0.85	0.35	1.65	2.67	3.03	1.53	1.51	-0.15
0.95	0.39	0.624	1.14	1.61	1.60	1.57	-0.12
1.05	0.42	0.218	0.373	0.568	1.68	1.63	-0.08
1.15	0.46	0.081	0.159	0.241	1.75	1.68	-0.04

Table 6: Basic numbers for DESI. The shell volume V is in units of $(\text{Gpc}/h)^3$, while the number density N_X for the tracers X (LRGs, ELGs, QSOs) is in $10^{-4} (h/\text{Mpc})^3$. The corresponding fiducial value for b_{10}^X and the estimates of ν_X and the non-linear bias b_{20}^X are also presented.

z	V	N_{ELG}	b_{10}^{ELG}	ν_{ELG}	b_{20}^{ELG}	N_{LRG}	b_{10}^{LRG}	ν_{LRG}	b_{20}^{LRG}	N_{QSO}	b_{10}^{QSO}	ν_{QSO}	b_{20}^{QSO}
0.15	0.23	23.0	0.91	0.85	-0.21	3.06	1.84	1.74	0.02	0.489	1.30	1.31	-0.22
0.25	0.56	8.65	0.96	0.92	-0.22	3.12	1.94	1.81	0.09	0.574	1.37	1.37	-0.21
0.35	0.98	4.15	1.01	0.99	-0.23	3.17	2.04	1.88	0.18	0.442	1.44	1.44	-0.19
0.45	1.45	2.76	1.06	1.06	-0.23	3.21	2.15	1.95	0.29	0.300	1.52	1.50	-0.16
0.55	1.93	3.13	1.12	1.12	-0.23	3.26	2.26	2.01	0.41	0.233	1.59	1.56	-0.13
0.65	2.40	4.22	1.17	1.18	-0.23	3.29	2.37	2.08	0.55	0.199	1.67	1.62	-0.08
0.75	2.84	5.48	1.23	1.24	-0.23	3.32	2.49	2.15	0.70	0.182	1.76	1.68	-0.04
0.85	3.26	5.73	1.29	1.30	-0.22	2.03	2.61	2.21	0.87	0.189	1.84	1.74	0.02
0.95	3.63	5.40	1.35	1.35	-0.21	0.35	2.73	2.28	1.06	0.193	1.93	1.80	0.09
1.05	3.97	5.19	1.41	1.41	-0.20	0.04	2.85	2.34	1.26	0.198	2.01	1.86	0.16
1.15	4.26	4.87	1.47	1.46	-0.18	0	0	0	0	0.204	2.10	1.92	0.24
1.25	4.52	4.40	1.53	1.51	-0.15	0	0	0	0	0.214	2.19	1.97	0.33
1.35	4.74	3.31	1.59	1.56	-0.13	0	0	0	0	0.222	2.27	2.02	0.43
1.45	4.93	2.20	1.65	1.61	-0.10	0	0	0	0	0.230	2.36	2.08	0.54
1.55	5.09	1.27	1.72	1.66	-0.06	0	0	0	0	0.228	2.45	2.13	0.65
1.65	5.22	0.480	1.78	1.70	-0.02	0	0	0	0	0.215	2.54	2.18	0.78
1.75	5.33	0.129	1.84	1.75	0.02	0	0	0	0	0.202	2.63	2.23	0.91
1.85	5.41	0	0	0	0	0	0	0	0	0.191	2.72	2.28	1.05

Table 7: Basic numbers for Euclid. The shell volume V is in units of $(\text{Gpc}/h)^3$, while the number density N in $10^{-4} (h/\text{Mpc})^3$. The fiducial value for b_{10} and the estimates of ν and the non-linear bias b_{20} are also presented.

z	V	N	b_{10}	ν	b_{20}
0.65	2.57	6.42	1.06	1.06	-0.23
0.75	3.05	14.5	1.11	1.12	-0.23
0.85	3.49	16.3	1.17	1.18	-0.23
0.95	3.89	15.0	1.22	1.23	-0.23
1.05	4.25	13.3	1.27	1.29	-0.22
1.15	4.57	11.6	1.33	1.34	-0.21
1.25	4.84	10.1	1.38	1.39	-0.20
1.35	5.08	8.42	1.44	1.44	-0.19
1.45	5.28	6.68	1.50	1.48	-0.17
1.55	5.45	5.09	1.55	1.53	-0.14
1.65	5.59	3.69	1.61	1.58	-0.12
1.75	5.71	2.56	1.67	1.62	-0.09
1.85	5.80	1.68	1.73	1.66	-0.05
1.95	5.87	1.02	1.78	1.70	-0.02
2.05	5.93	0.380	1.84	1.74	0.02